Climatic and hydrologic variability in the northern Mediterranean across the onset of the Messinian salinity crisis

Published version:

DOI:10.1016/j.palaeo.2020.109632

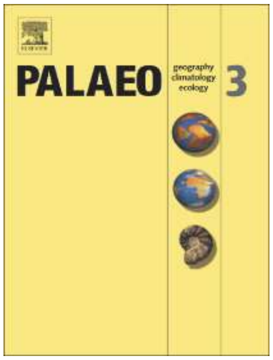

Climatic and hydrologic variability in the northern Mediterranean across the onset of the Messinian salinity crisis

Mathia Sabino, Enno Schefuß, Marcello Natalicchio, Francesco Dela Pierre, Daniel Birgel, David Bortels, Bernhard Schnetger, Jörn Peckmann

PII: S0031-0182(20)30076-6

DOI: https://doi.org/10.1016/j.palaeo.2020.109632

Reference: PALAEO 109632

To appear in: *Palaeogeography, Palaeoclimatology, Palaeoecology*

Received date: 11 October 2019

Revised date: 28 January 2020

Accepted date: 29 January 2020

Please cite this article as: M. Sabino, E. Schefuß, M. Natalicchio, et al., Climatic and hydrologic variability in the northern Mediterranean across the onset of the Messinian salinity crisis, *Palaeogeography, Palaeoclimatology, Palaeoecology* (2020), https://doi.org/10.1016/j.palaeo.2020.109632

Climatic and hydrologic variability in the northern Mediterranean across the onset of the Messinian salinity crisis

Mathia Sabino[a], Enno Schefuß[b], Marcello Natalicchio[c], Francesco Dela Pierre[c], Daniel Birgel[a*], David Bortels[a], Bernhard Schnetger[d], Jörn Peckmann[a]

[a]*Institut für Geologie, Centrum für Erdsystemforschung und Nachhaltigkeit, Universität Hamburg, D-20146 Hamburg, Germany*

[b]*MARUM – Zentrum für Marine Umweltwissenschaften, Universität Bremen, D-28359 Bremen, Germany*

[c]*Dipartimento di Scienze della Terra, Università degli Studi di Torino, I-10125 Torino, Italy*

[d]*Institut für Chemie und Biologie des Meeres, Universität Oldenburg, D-26111 Oldenburg, Germany*

*Corresponding author

Postal address: Universität Hamburg, Institut für Geologie, Bundesstraße 55, 20146 Hamburg, Germany

E-mail address: daniel.birgel@uni-hamburg.de

Keywords: paleoclimate, major and trace elements, plant waxes, *n*-alkanes, hydrogen isotopes, stable carbon isotopes

ABSTRACT

The youngest and one of the largest saline deposits of Earth history formed in the Mediterranean during the Messinian salinity crisis (MSC; 5.97 - 5.33 Ma, Late Miocene), when global climate was experiencing a trend of cooling and aridification. However, recent paleoclimate reconstructions indicate strong climate gradients across the Mediterranean Basin and the persistence of humid conditions in the northern Mediterranean during the earliest phase of the MSC. To characterize climatic and hydrologic variability across the onset of the MSC, we studied inorganic geochemical proxies, comprising Si, Ti, and Zr element distributions and organic geochemical proxies, such as sedimentary plant wax contents and their carbon ($\delta^{13}C_{n\text{-alk}}$) and hydrogen ($\delta^{2}H_{n\text{-alk}}$) stable isotope compositions in deep-water (>200 m), alternating shale and marl deposits of the Piedmont Basin (Govone section; NW Italy). Our results suggest that deposition was controlled by precession-driven climate fluctuations before and after the onset of the MSC, with shales deposited under moister conditions (lower element/Al ratios and $\delta^{2}H_{n\text{-alk}}$ values) and marls when drier conditions prevailed (higher element/Al ratios and $\delta^{2}H_{n\text{-alk}}$ values). The observed $\delta^{2}H_{n\text{-alk}}$ pattern further suggests changes in the relative contributions of the sources of moisture for precipitation. At precession minima, shales were deposited and moisture was mainly sourced from the North Atlantic, as reflected by lower $\delta^{2}H_{n\text{-alk}}$ values. At precession maxima, marls were deposited and higher $\delta^{2}H_{n\text{-alk}}$ values point to a – probably western – Mediterranean source of moisture. The decrease of element/Al ratios as well as the coeval increase of plant wax abundances after the onset of the MSC indicate enhanced humidity and increased net precipitation over the northern Mediterranean. These changes coincided with a restriction of the Atlantic-Mediterranean gateways and resulted from an enhanced contribution of deuterium-enriched moisture sourced from seawater evaporation in the Mediterranean, evidenced by an increase of $\delta^{2}H_{n\text{-alk}}$ values.

1. Introduction

Following the Mid-Miocene Climatic Optimum, the global climate experienced a trend of cooling and aridification, coinciding with evidence for transient glaciations in the northern Hemisphere and the establishment of a marked seasonality (e.g. Herbert et al., 2016; Pound et al., 2012; Tzanova et al., 2015; Zachos et al., 2001). This trend culminated in the Late Miocene (between 7 and 5.3 Ma) in the decrease of ocean temperatures to modern values (Herbert et al.,

2016) and was accompanied by changes in terrestrial ecosystems. One prominent change was the expansion of C_4-dominated grasses at the expenses of C_3 grasslands (Cerling et al., 1997; Hötzel et al., 2013; Strömberg, 2011). In the Mediterranean area, the Late Miocene cooling coincided in part with the so-called Messinian salinity crisis (MSC, 5.97 – 5.33 Ma; Manzi et al., 2013). The MSC represents an environmental crisis during which the Mediterranean was transformed into the youngest salt giant in Earth history (Cita et al., 1978; Flecker et al., 2015; Hsü et al., 1973; Roveri et al., 2014). This event is thought to have been driven by the progressive restriction of the Atlantic-Mediterranean gateways (e.g. Flecker et al., 2015; Krijgsman et al., 2018), superimposed by long (eccentricity) and short (precession) orbitally-controlled climate fluctuations (Roveri et al., 2014), modulating the hydrological budget of the basin (Meijer and Tuenter, 2007; Simon et al., 2017). Part of the MSC stratigraphic record is typified by a precession-paced cyclic succession of shales, diatomites, and marls, with shales recording humid conditions at precession minima and insolation maxima and marls recording more arid conditions at precession maxima and insolation minima (Bellanca et al., 2001; Blanc-Valleron et al., 2002; Gennari et al., 2018; Hilgen and Krijgsman, 1999; Kouwenhoven et al., 2006; Lozar et al., 2018; Manzi et al., 2007; Sierro et al., 1999). During the first phase of the MSC, shale and gypsum couplets of the Primary Lower Gypsum unit (PLG; Roveri et al., 2008) were deposited in shallow peripheral basins (<200 m), changing laterally to shale and marl cycles similar to their pre-MSC counterparts in basins of intermediate to deep water depths (>200 m; e.g. Dela Pierre et al., 2011; Manzi et al., 2007; Natalicchio et al., 2019). The evaporite cycles and their lateral equivalents reflect precession-controlled fluctuations of the Mediterranean climate (Krijgsman et al., 1999; Natalicchio et al., 2019), with gypsum depositing in marginal settings and marls in intermediate to deep settings. The deposition of gypsum and marls corresponds to precession maxima and periods of more arid conditions, reflecting a reduced net hydrological budget of the basin (Roveri et al., 2014).

The widespread deposition of evaporites during the MSC was originally taken as the main argument for aridification of the whole Mediterranean area (Hsü et al., 1973). However, later reconstructions indicated no substantial climate change across the onset of the MSC and revealed that strong latitudinal gradients persisted in the Mediterranean with a wet northern region and an arid southern region (Bertini, 2006; Bertini and Martinetto, 2011, 2008; Fauquette et al., 2006; Favre et al., 2007; Jiménez-Moreno et al., 2013, 2010; Suc and Bessais, 1990). Such reconstructions were mostly based on pollen and plant remains, which are, however, scarce and poorly preserved within evaporites (Bertini, 2006; Bertini and Martinetto, 2011; Fauquette et al., 2006).

An alternative approach to reconstruct climate variability involves the application of inorganic and organic geochemical proxies such as major and trace elements (Calvert and Pedersen, 2007; Schnetger et al., 2000; Tribovillard et al., 2006; Wehausen and Brumsack, 2000, 1999) and sedimentary long chain *n*-alkanes and their carbon and hydrogen stable isotopic compositions (Eglinton and Eglinton, 2008; Naafs et al., 2012; Pancost and Boot, 2004; Pedentchouk and Zhou, 2018; Schefuß et al., 2005, 2003; Tipple and Pagani, 2010; Vasiliev et al., 2017, 2015). Long-chain *n*-alkanes are common constituents of epicuticular waxes of terrestrial higher plants (e.g. Diefendorf et al., 2011; Eglinton and Hamilton, 1967). Due to their refractory nature, they are excellent recorders of climate-induced change in terrestrial vegetation and input of terrestrial organic matter (TOM) to ocean basins (e.g. Pancost and Boot, 2004; Schefuß et al., 2003).

Here, we use geochemical proxies to study the onset of the MSC archived in the Govone section (Piedmont Basin, NW Italy), aiming for the reconstruction of changes in climate, terrestrial vegetation (C_3 vs C_4 plants), and hydrology at the northernmost offshoot of the Mediterranean Basin. The MSC is reflected at this location by a cyclic succession of shales and marls, representing the deep water equivalent of the PLG unit (Bernardi, 2013; Dela Pierre et al., 2016). Our study documents the presence of humid climate conditions in the northern sectors of the Mediterranean during the earliest phase of the MSC. Moreover, the new data complement climate and few hydrological reconstructions from other Mediterranean regions (Andersen et al., 2001; Vasiliev et al., 2017, 2015, 2013), confirming the presence of strong climate gradients across the Mediterranean during the MSC.

2. Geological and stratigraphic setting

2.1 The Piedmont Basin

The Piedmont Basin is a wedge-top basin filled with upper Eocene to Messinian sediments that developed in the Alpine retroforeland and became eventually involved in the Apennine orogeny (Mosca et al., 2010; Rossi, 2017; Rossi and Craig, 2016; Fig. 1A). The Messinian sediments, mostly buried beneath Pliocene to Quaternary deposits of the Savigliano and Alessandria sub-basins (Irace et al., 2005), are exposed along the uplifted southern and northern basin margins (Dela Pierre et al., 2011; Fig. 1A). The succession starts with alternating organic-rich shales and marls deposited in an outer shelf to slope environment (Sant'Agata Fossili Marls, Tortonian – lower Messinian; Sturani, 1973; Fig. 1B), forming 2 to 3 m thick lithological cycles. Abundance fluctuation of calcareous microfossil assemblages demonstrated that lithological cyclicity was controlled by precession-controlled climate change, with shales recording moister climate at precession minima and insolation maxima and marls reflecting drier climate at precession maxima and insolation minima (Lozar et al., 2018; Violanti et al., 2013). At the southern and northern basin margins, the Sant'Agata Fossili Marls are overlain by sulfate evaporites of the PLG unit deposited during the first stage of the MSC (Fig. 1B; Dela Pierre et al., 2011). Basinward, the gypsum layers of the PLG unit laterally pass into marls alternated with organic-rich shales (Dela Pierre et al., 2011; Natalicchio et al., 2019, 2017; Fig. 1B). The PLG unit and its lateral, deeper equivalents are unconformably overlain by resedimented and chaotic evaporites (Valle Versa Chaotic Complex; Dela Pierre et al., 2007; Irace et al., 2005), equivalent to the Resedimented Lower Gypsum unit deposited in many Mediterranean sub-basins during the second stage of the MSC (5.60-5.55 Ma; Roveri et al., 2014). The Messinian succession ends with fluvio-deltaic and lacustrine deposits, characterized by brackish water fauna of the Lago Mare biofacies (Cassano Spinola Conglomerates;

Dela Pierre et al., 2011; Sturani, 1976; Fig. 1B), recording the third stage of the MSC (5.55-5.33 Ma; Roveri et al., 2014).

2.1.1 The Govone section

The Govone section (44°48′08″N; 8°07′34″E) is located at the southwestern margin of the Piedmont Basin (Fig. 1A, B) and comprises the entire Messinian succession (Bernardi, 2013; Bernardi et al., 2012; Dela Pierre et al., 2016). Here, the Sant'Agata Fossili Marls comprise 35 lithological cycles (Gm1 – Gm35; Fig. 2) composed of shale and marl couplets with up to 2 m thickness (Fig. 1C, D, E). The upper cycles (Gm33 to Gm35) are disturbed to some extent by slumping. The Sant'Agata Fossili Marls are conformably overlain by the PLG unit, which is composed of nine lithological cycles (Gg1 – Gg9; Fig. 2). Gypsum beds are up to 3 m thick and are made up of laminar gypsum, consisting of alternating clay-rich and gypsum-rich laminae. In some layers, flattened conical structures, composed of mm to cm-sized selenite crystals are present. They are interpreted as poorly developed branching selenite (*sensu* Lugli et al., 2010), whose growth was hampered by clay deposition (Dela Pierre et al., 2016). The PLG unit is overlain by clastic gypsum layers interbedded to laminated shales (Valle Versa Chaotic Complex; Dela Pierre et al., 2016). The Messinian succession terminates with fluvio-deltaic deposits (Cassano Spinola Conglomerates; Dela Pierre et al., 2016).

2.1.2 The MSC onset in the Govone section

The age model for the Govone section (Bernardi, 2013) is based on the identification of several age-diagnostic planktonic foraminifer bioevents correlated with the astronomically tuned Perales reference section (Manzi et al., 2013; Sierro et al., 2003, 2001). The most diagnostic bioevents identified by Bernardi (2013) and used for astrochronological correlations are: (1) the first abundant occurrence of *Turborotalita multiloba* in cycle Gm12, which is dated 6.415 Ma in the Perales section (Sierro et al., 2001); (2) the left/right coiling change of *Neogloboquadrina acostaensis* in cycle Gm14, recorded in cycle UA17 at Perales and dated at 6.36 Ma (Sierro et al., 2001); (3) the 1st influx of *Globorotalia scitula* in cycle Gm17, dated at 6.29 Ma in Perales (Sierro et al., 2001). A hiatus of about 50 kyr (approximately three precessional cycles), corresponding to a slump scar, was identified in the marls of cycle Gm17, immediately above this last bioevent (Bernardi, 2013); (4) a 2nd influx of *G. scitula* in cycle Gm24, which occurs within an acme interval of *T. multiloba*. This acme interval was reported in Perales between cycles UA23 and UA30 (Sierro et al., 2001). Consequently, the 2nd influx of *G. scitula* in cycle Gm24 is correlated with that recognized in Perales in cycle UA29 and dated at 6.10 Ma (Sierro et al., 2001). Accordingly, the onset of the MSC – corresponding to the timeline at 5.97 Ma – was placed in the Govone section at the base of the marls of cycle Gm30, i.e. six precession cycles above the 2nd influx of *G. scitula* (Bernardi, 2013). Correlation with the Perales reference section indicates that the marls of cycle Gm30 correspond to the first gypsum bed of Perales (cycle PLG1, Manzi et al., 2013), which appears six cycles above the 2nd influx of *G. scitula* (Fig. 2A). In the Govone section, calcareous microfossils disappear in the marls of cycle Gm27, probably because of diagenetic processes favoring dissolution of calcareous tests (Bernardi, 2013). The disappearance of calcareous tests prevents the recognition of the calcareous nannofossil biovents (abundance peak of *Sphenolithus abies*, followed by minor peaks of *Helicosphaera carteri* and *Umbilicosphaera rotula*) that were used to approximate the onset of the MSC in the absence of evaporites in different Mediterranean sub-basins (Gennari et al., 2018; Lozar and Negri, 2019) including the Piedmont basin (Pollenzo section; Lozar et al., 2018). The position proposed by Bernardi (2013) an herein for the onset of the MSC does not correspond to the position reported by Dela Pierre et al. (2016), who placed the MSC onset one cycle below, i.e. cycle Gm29. The latter misplacement reflected an error in the bed by bed correlation of the upper part of the Govone section with the Perales section. Consequently, the work of Dela Pierre et al. (2016) should not be used as a reference for the age model of the Govone section. In the topmost part of the Sant'Agata Fossili marls, the presence of slumps makes the identification of the cyclostratigraphic pattern problematic. However, it is still possible to recognize undeformed layers of organic-rich shales that correspond to the lower part of the three lithological cycles (Gm 33, Gm34 and Gm 35) immediately below the gypsum-bearing cycles of the PLG unit (Fig. 2A).

To sum up, in the Govone section the onset of the MSC was identified in the upper part of the Sant'Agata Fossili Marls (Fig. 2A). The studied section includes four pre-MSC cycles (Gm26 – Gm29) and four MSC cycles (Gm30 – Gm33; Fig. 2B), the latter corresponding to the deep-water counterparts of the lower four PLG cycles exposed in the marginal part of the basin, with marls interpreted as lateral equivalents of gypsum (cf. Bernardi, 2013).

3 Materials and methods

Thirty-three excavated samples (four samples per cycle on average) were collected from cycles Gm26 to Gm33. For each sample an aliquot was dried and homogenized with an agate mortar. The obtained powders were divided in sub-aliquots to perform the analyses described below.

3.1 X-ray fluorescence (XRF) analyses

All samples were analyzed by X-ray fluorescence (XRF) for major and trace element contents at the Institute of Chemistry and Biology of the Marine (ICBM) Environment of the University of Oldenburg using an Axios plus, Panalytical spectrometer. Di-lithium tetraborate (4.2 g) and ammonium nitrate (1 g) for preoxidation were added to 0.7 g of samples and then fused to glass beads. An in-house black shale reference material and international standard were used to check analytical accuracy, which was ≤0.3% for major (Al, Si, Ti) and ≤4% for trace (Zr) elements. Silicon, Ti and Zr were plotted against Al to assess relative enrichment or depletion with respect to the background aluminosilicates of the investigated marls and shales (Calvert and Pedersen, 2007; Tribovillard et al., 2006). Ratios were calculated from wt%/wt% for Si/Al and Ti/Al and from (mg/kg)/wt% for Zr/Al.

3.2 Total organic and inorganic carbon contents

The total inorganic (TIC) and organic (TOC) carbon contents were measured at the Institute for Geology of the University of Hamburg. The sub-aliquots were further split into two fractions. One fraction was used to determine total carbon (TC) contents using a LECO SC-144DR Carbon Analyzer equipped with an infrared detector, heating the sample to 1350°C. The other fraction was heated to 550°C for 5 h to combust the organic carbon (OC) fraction, before temperature was raised to 1350°C to determine total inorganic carbon (TIC) contents. Prior and after sample analysis, a Synthetic Carbon Leco 502-029 (1.01 ± 0.02 carbon%) standard was measured. TOC contents were determined with the formula $TOC = TC - TIC$.

3.3 Lipid biomarker analyses

Twenty-one samples were selected for lipid biomarker analyses (at least 2 samples per cycle) following the procedure described in Birgel et al. (2006). The total lipids where extracted by saponification with 6% potassium hydroxide in methanol in an ultrasonic bath (80°C/2h), followed by repeated ultrasonication with dichloromethane(DCM):methanol (3:1, v:v) until the organic solvent phase became colorless. To transfer also the released fatty acids after saponification (not further discussed in this study) to the organic solvent phase, extracts were treated with pure water and 10% hydrochloric acids to reach pH 2. The organic solvent phase with the extracts was reduced through a rotary evaporator, transferred into vials with DCM and dried. To prepare the extracts for gas chromatography (GC) analyses, a cleaning procedure was applied: the vials containing the total lipid extracts were washed with *n*-hexane to separate the *n*-hexane-soluble fraction (collected in a separate vial) from the dichloromethane-soluble fraction. The former was further split in four sub-fractions of increasing polarity (hydrocarbons, ketones, alcohols and carboxylic acids) via solid phase extraction using a Supelco glass cartridge (6 ml, 500 mg, DSC-NH_2). The hydrocarbon fraction was eluted with *n*-hexane and finally dried. For GC analysis, *n*-hexane was used as eluent. Compounds were identified with a Thermo Scientific Trace GC Ultra coupled to a Thermo Scientific DSQ II mass spectrometer (GC-MS) through comparison of retention times and published mass spectral data. A Fisons Instruments GC 8000 series equipped with a flame-ionization detector (GC-FID) was used for compound quantification. For the hydrocarbon fraction, 5α-cholestane was used as internal standard for quantification. Helium was used as carrier gas for GC-MS runs, while for GC-FID analyses hydrogen was used. An Agilent HP-5MS UI fused silica column with a length of 30 m, a diameter of 0.25 mm, and a film thickness of 0.25 μm was used for all analyses. The GC temperature program was: 50 °C (3 min); from 50 °C to 230 °C (held 2 min) at 25 °C/min; from 230 °C to 320 °C (held 20 min) at 6°C/min.

3.3.1 Compound-specific hydrogen and carbon stable isotopes

Compound-specific stable hydrogen (δ^2H; sixteen samples) and carbon ($\delta^{13}C$; twenty-one samples) isotope analyses of long-chain *n*-alkanes were performed at MARUM – Center for Marine Environmental Sciences, University of Bremen and Institute for Geology at Hamburg University, respectively.

Hydrogen isotopes were measured using a ThermoFisher Scientific Trace GC coupled via a pyrolysis reactor (operated at 1420 °C) to a ThermoFisher Scientific MAT 253 isotope mass spectrometer (GC-IRMS). The GC temperature program was: 120 °C held for 3 min, heating up to 320 °C with a rate of 5 °C/min and then held for 15 min. δ^2H values were calibrated against H_2 external reference gas and are reported in ‰ versus Vienna Standard Mean Ocean Water (V-

SMOW). The H^{3+}-factor varied from 5.05 to 5.14 during the measurement period. After every six runs an externally calibrated standard mixture of 16 *n*-alkanes was measured. Its long-term precision and accuracy were 3‰ and <1‰, respectively. Analyses were conducted in duplicate when *n*-alkane concentrations were high enough. Average reproducibility in replicate analyses of the *n*-C_{31} and *n*-C_{33} alkanes was 1.1‰ and 1.8‰, respectively. Measurement of *n*-C_{29} alkane δ^2H values was impossible due to coelution with the internal standard (5α-cholestane).

Carbon isotopes were measured using an Agilent 6890 GC coupled via a Thermo Finnigan Combustion III to a Thermo Finnigan Delta Plus XL isotope mass spectrometer (GC-IRMS). The temperature program was: 50 ºC held for 2 min, heating up to 320 ºC with a rate of 12 ºC/min and held for 35 min. $\delta^{13}C$ values are reported in ‰ versus Vienna Pee Dee Belemnite (V-PDB). After every 3 to 4 samples, an externally calibrated standard mixture of 15 *n*-alkanes was measured. Analyses were conducted at least in duplicates when *n*-alkanes concentrations were high enough. Average reproducibility in replicate analyses of the *n*-C_{31} and *n*-C_{33} alkanes was 0.3‰ and 0.4‰, respectively. $\delta^{13}C$ values of *n*-C_{29} alkane were not considered because of coelution with the internal standard.

3.3.2 Carbon Preference Index

The odd-over-even predominance of higher plants derived *n*-alkanes was calculated through the Carbon Preference Index (CPI), according to the formula from Bray and Evans (1961):

$$\mathrm{CPI}=0.5\times\left(\frac{C_{25}+C_{27}+C_{29}+C_{31}+C_{33}}{C_{24}+C_{26}+C_{28}+C_{30}+C_{32}}+\frac{C_{25}+C_{27}+C_{29}+C_{31}+C_{33}}{C_{26}+C_{28}+C_{30}+C_{32}+C_{34}}\right) \tag{1}$$

where C_n indicates the relative concentrations of C_{24} to C_{34} *n*-alkanes. CPI values in sediments can be used to trace the level of degradation and/or contamination of the terrestrial organic matter, with low values (CPI ≤2) indicating diagenetic/catagenetic degradation (e.g. Mayser et al., 2017; Pancost and Boot, 2004) and/or contamination from recycled and degraded organic matter from older sediments (Cortina et al., 2016).

4 Results

4.1 Lithological cycles, major and trace element distribution, and total organic carbon

The studied section consists of lithological cycles of shale and marl couplets ranging in thickness from 50 cm to 1 m (Fig. 1C, D, E, 3). The laminated shales are dark gray to olive (Fig. 1D), while marls are light gray and homogeneous (Fig. 1E); in the pre-MSC cycles (except for cycle Gm29) marls are bioturbated. Estimates on sedimentation rates are obtained by dividing the thickness of each cycle by the time of deposition and vary between 2.3 cm/kyr and 4.9 cm/kyr, with slightly higher average sedimentation rates in the MSC interval (4.1 cm/kyr) than in the pre-MSC cycles (3.1 cm/kyr; see Supplementary material). No sedimentation rates are assessed for cycle Gm33 because of a slumped interval at its top.

The Ti/Al, Si/Al, and Zr/Al ratios display a distinct cyclic pattern with a narrow amplitude. Lower values are found for shales and higher values for marls (Fig. 3; see Supplementary material), although locally this pattern is partially blurred, particularly for the Si/Al ratio (Gm31-Gm32 cycles; see paragraph 5.1 for a discussion). Overall, the ratios slightly decrease from the pre-MSC to the MSC intervals (Fig. 3).

The total organic carbon (TOC) contents vary in accord with lithological cyclicity, with higher contents (up to 3.1%) found for shales and lower contents (as low as 1.0%) obtained for marls (Supplementary material).

4.2 *n*-Alkane distributions and Carbon Preference Index (CPI)

The *n*-alkanes found in the Govone samples range from C_{18} to C_{37} with a strong odd-over-even predominance (Fig. 4). The most abundant homologues are the *n*-C_{31} and *n*-C_{29} alkanes, followed by *n*-C_{27} and *n*-C_{33} (Fig. 4; Supplementary material). Longer homologues, i.e. *n*-C_{35} and *n*-C_{37}, were also detected. However, *n*-C_{35} coelutes with lycopane (Fig. 4), a compound whose source is still uncertain (Sinninghe Damsté et al., 2003; Wakeham et al., 1993), while *n*-C_{37} occurs only in trace amounts. Short chain *n*-alkanes (*n*-C_{18-23}) show commonly very low abundances (< 1.5 μg/g TOC). The contents of long chain *n*-alkanes (C_{27}, C_{29}, C_{31} and C_{33}) mirror lithological cyclicity, with highest contents in shales (up to 156 μg/g TOC) and lowest contents in marls (as low as 10 μg/g TOC). After the MSC onset, contents of long-chain *n*-alkanes increase (Fig. 3), reflected by an almost doubling of average contents from the pre-MSC (34 μg/g TOC) to the MSC cycles (58 μg/g TOC).

The CPI ranges from 4.3 to 7.7 with highest values in shales (Fig. 3; Supplementary material). Lower average CPI values (pre-MSC: 6.2; MSC: 5.4; Supplementary material) are found after the onset of the MSC (Fig. 3). The CPI values are persistently >4 and show that sedimentary TOM is largely unaffected by recycled organic matter. The pronounced cyclicity reflecetd in proxy patterns suggests that aging of leaf waxes in soils is negligible (e.g. Aichner et al., 2018; Eglinton et al., 1997), indicating that possible temporal biases are smaller than the temporal spacing of sample intervals (minimum temporal spacing for biomarker analyses of ∼2 kyr and ∼3 kyr for pre-MSC and MSC, respectively).

4.2.1 *n*-Alkanes – carbon and hydrogen isotopes ($\delta^{13}C$ and $\delta^{2}H$ values)

The $\delta^{13}C$ values of *n*-C_{31} and *n*-C_{33} alkanes vary from −33.7‰ to −30.2‰, without a pattern depending on lithology (Fig. 3; Supplementary material). On average, $\delta^{13}C$ values slightly decrease in MSC sediments ($\delta^{13}C_{31\text{-alk}}$: −32.4‰; $\delta^{13}C_{33\text{-alk}}$: −32.3‰) compared to pre-MSC sediments ($\delta^{13}C_{31\text{-alk}}$: −31.7‰; $\delta^{13}C_{33\text{-alk}}$: −31.3‰; Fig. 3; Supplementary material). The δ^2H values of the *n*-C_{31} and *n*-C_{33} alkanes range from −191‰ to −140‰, yielding a cyclic pattern in phase with lithology. Shales are characterized by ^2H-depletion compared to marls (Fig. 3; Supplementary material). Moreover, a shift toward higher δ^2H values is observed in the MSC interval, mainly caused by stronger ^2H-enrichment in shales (Fig. 3).

5 Discussion

5.1 Implications of changing elemental abundances

Fluctuations of Ti/Al, Si/Al, and Zr/Al ratios in marine sediments are commonly used as climate proxies. These element patterns allow to distinguish between arid phases, where aeolian input prevails, and humid phases characterized by dominant fluvial input (Calvert and Fontugne, 2001; Calvert and Pedersen, 2007; Martinez-Ruiz et al., 2015; Moller et al., 2012; Natalicchio et al., 2019; Schnetger et al., 2000; Wehausen and Brumsack, 2000, 1999). During arid phases, Ti is transported by wind in the detrital silt-sized fraction in the form of heavy minerals such as rutile, sphene, and ilmenite, resulting in an increase of the Ti/Al ratio in marine sediments (Moller et al., 2012; Schnetger et al., 2000; van der Laan et al., 2012). During humid climate phases, the Ti/Al ratio in marine sediments decreases due to higher fluvial input of clay minerals containing Al and a denser terrestrial vegetation cover, favoring chemical weathering – sink of Ti minerals – and lowering the deflation potential of the land surface (Moller et al., 2012; Schnetger et al., 2000). Similarly, Si/Al and Zr/Al ratios can be used to trace increased aeolian input, since wind derived material like loess is enriched in quartz and zircon, which are resistant to chemical and physical weathering (Schnetger, 1992; Wehausen and Brumsack, 1999).

In the Govone section, fluctuation of element abundances follows lithological cyclicity (Fig. 3), although in places this pattern is partially blurred, particularly the Si/Al ratio (Gm31-Gm32 cycles). The most likely reason for the latter is enrichment of biogenic silica (e.g. Calvert and Pedersen, 2007) or authigenic minerals derived from dissolution and reprecipitation of biogenic silica (Badaut and Risacher, 1983; Schieber, 1996), which can bias climate reconstructions. Therefore, when using the Si/Al ratio as paleoclimate proxy, this approach must be validated by other proxies such as Ti/Al and Zr/Al ratios or the distribution of land-derived lipids (e.g. *n*-alkanes). Despite some variability, the lower Ti/Al, Zr/Al, and Si/Al ratios of shales agree with more humid conditions, whereas the higher element/Al ratios in marls suggest increased aeolian transport during more arid phases. Interestingly, a trend to lower ratios after the MSC onset suggests that the supply of heavy minerals and quartz, representing sources of Ti, Zr, and Si, weakened and input of clay minerals, representing a source of Al, apparently increased. Both scenarios agree with an increase of humidity during the early phase of the MSC, in line with recent reconstructions for northern, marginal sectors of the Mediterranean (Natalicchio et al., 2019). Humid to arid climate oscillations have already been recognized in the pre-MSC cycles of Govone (Bernardi, 2013) and other parts of the Mediterranean (e.g. Blanc-Valleron et al., 2002; Gennari et al., 2018; Kouwenhoven et al., 2006; Lozar et al., 2018; Sierro et al., 2003) based on changes in calcareous plankton assemblages attributed to precessional forcing. The cyclic element patterns described above confirm that the deposition of the microfossil deprived (pre-MSC) and apparently microfossil free (MSC) Govone strata was controlled by precession, with shales reflecting more humid phases at precession minima (insolation maxima) and marls reflecting more arid phases at precession maxima (insolation minima; see also Natalicchio et al., 2019 for the neigbouring Pollenzo section).

5.2 Controls of climate on input of terrestrial organic matter (TOM)

Long-chain *n*-alkanes (C_{27-33}) are lipid biomarkers predominantly sourced by epicuticular leaf waxes of terrestrial vascular plants (Eglinton and Hamilton, 1967; Eglinton and Eglinton, 2008). Their highly refractory nature to degradation in the water column and sediments (Diefendorf and Freimuth, 2017) makes them excellent proxies for tracing the input of terrestrial organic matter (TOM) to the sediment (Diefendorf and Freimuth, 2017; Mayser et al., 2017; Pancost and Boot, 2004; Pedentchouk and Zhou, 2018; Schefuß et al., 2003; Vasiliev et al., 2019, 2017). Higher contents of long-chain *n*-alkanes in the shales than in marls of the Govone section suggest that TOM input was controlled by precession. The high CPI values (>4) and the observed *n*-alkanes distribution confirm that plant waxes were mostly sourced by coeval terrestrial vegetation of the Piedmont Basin hinterland through fluvial transport, while aeolian transport was apparently of only minor importance (cf. Natalicchio et al., 2019). Taken together, such patterns confirm that TOM input was higher during humid phases at insolation maxima, corresponding to times of shale deposition and low element/Al ratios. Moister conditions favored the growth of vegetation in the hinterland and triggered more intense riverine runoff (Natalicchio et al., 2019), resulting in higher contents of long chain *n*-alkanes in shales. At times of marl deposition during more arid phases dominated by aeolian transport, the input of TOM and river discharge were significantly reduced (cf. Natalicchio et al., 2019).

Apart from the variability between the different lithologies, a general increase of long chain *n*-alkane contents occurred after the onset of the MSC (Fig. 3). Such increase may reflect progressive shallowing of the basin along with a displacement of the coastline toward the basin depocenter or an increase of humidity, resulting in denser vegetation and more transport of TOM to the basin. Since neither sedimentological characteristics, nor geological regional reconstructions (e.g. Dela Pierre et al., 2011) indicate abrupt shallowing, the increase of *n*-alkane contents and the lowering of CPI values rather point to a shift toward more humid conditions after the advent of the crisis. Such change toward moister conditions enhanced (1) soil weathering and the associated degradation of plant waxes in soils (Luo et al., 2012) and (2) riverine runoff and transport of TOM to the basin.

This scenario is consistent with the observed increase of sedimentation rates from the pre-MSC (3.1 cm/kyr on average) to the MSC interval (4.1 cm/kyr on average).

5.3 Source of terrestrial organic matter: Insights from compound-specific carbon isotopes

The $\delta^{13}C_{31\text{-}33\text{-alk}}$ values obtained for the Govone section ranging from −33.7‰ to −30.2‰ indicate the predominance of C_3 vegetation in the hinterland of the Piedmont Basin. C_3 plants, mostly trees and shrubs adapted to cooler and humid conditions, use the Calvin-Benson-Bassham cycle and synthesize ^{13}C-depleted long chain *n*-alkanes ($\delta^{13}C_{n\text{-alk}} \sim -34‰$). Conversely, C_4 plants, mostly grasses adapted to warm and arid conditions, use the Hatch-Slack pathway and produce less ^{13}C-depleted lipids ($\delta^{13}C_{n\text{-alk}} \sim -21‰$; Collister et al., 1994; Naafs et al., 2012; Tipple and Pagani, 2010). The predominance of C_3 plants in the Messinian of the working area was already recorded using lipid biomarkers (Pollenzo section; Natalicchio et al., 2019), paleobotanical data (pollen and macrofossils), and paleovegetation models (Bertini, 2006; Bertini and Martinetto, 2011, 2008; Fauquette et al., 2006; Favre et al., 2007). All proxies indicate the predominance of arboreal C_3 plants, whereas herbs were very scarce at least during insolation maxima. According to Bertini and Martinetto (2011), land plants were mostly represented by subtropical humid taxa in lowlands and conifers in uplands. However, only the subtropical-humid taxa are likely sources of *n*-alkanes in the studied section; otherwise chain distribution pattern of *n*-alkanes would be different. The two main conifer families reported for the Piedmont Basin are *Pinaceae* and *Cupressaceae* (Bertini and Martinetto, 2011, 2008). *Pinaceae* produce very low amounts of plant waxes or even none (Diefendorf et al., 2015), whereas *Cupressaceae* produce abundant C_{33} to C_{37} odd-numbered *n*-alkanes (Diefendorf et al., 2015; Diefendorf and Freimuth, 2017). These *n*-alkanes are minor constituents in the Govone sediments, therefore conifers are at best a minor source of *n*-alkanes. The almost identical $\delta^{13}C_{n\text{-alk}}$ values in the marls relative to shales further suggest that subtropical C_3 plants still dominated at precession maxima even after the MSC onset. Since the MSC marls in intermediate to deep basins are considered as time equivalents of the marginal gypsum deposits (i.e. the PLG unit; Dela Pierre et al., 2011; Manzi et al., 2007; Natalicchio et al., 2019), our new data provide information on the type of vegetation at insolation minima during the first stage of the MSC; information that was not available before due to the absence of pollen and plant fossils in evaporites (cf. Bertini, 2006).

To sum up, little variability of $\delta^{13}C$ values of long chain *n*-alkanes in the Govone section point to the persistence of subtropical forests dominated by C_3 plants throughout the investigated interval (i.e. between 6.07 and 5.92 Ma). Furthermore, slightly lower $\delta^{13}C$ values in the upper part of the section probably reflect reduced water stress for C_3 plants caused by an increased humidity after the MSC onset. Reduced water stress decreased water use efficiency of plants, leading to enhanced isotope fractionation upon uptake of carbon dioxide and hence lower $\delta^{13}C$ values of leaf waxes (e.g. Diefendorf and Freimuth, 2017; Madhavan et al., 1991). Such pattern suggests that during the earliest phase of the MSC, the precession-paced climate in the northern Mediterranean never became arid as seen for the central or southern parts of the Mediterranean, which were instead dominated by an open, xeric vegetation (Bertini et al., 2006; Bertini and Martinetto, 2011, 2008; Fauquette et al., 2006; Favre et al., 2007; Suc and Bessais, 1990).

5.4 Hydrological changes across the onset of the MSC: Insights from compound-specific hydrogen isotopes

The $\delta^{2}H$ values of terrestrial plant *n*-alkanes ($\delta^{2}H_{n\text{-alk}}$) preserved in sediments represent a powerful tool for unraveling paleohydrological and paleoclimatic changes on continents (e.g. Andersen et al., 2001; Vasiliev et al., 2017, 2015). The hydrogen isotopic signature of plant *n*-alkanes mainly depends on the $\delta^{2}H$ value of meteoric water, the main hydrogen source for terrestrial plants (Sachse et al., 2012), and, to a lesser extent, on isotope enrichment due to evapotranspiration and water-use efficiency of the respective plant (Kahmen et al., 2013a, 2013b; Sachse et al., 2012;

Tipple and Pagani, 2010). In particular, ^{2}H-enrichment in waxes can result from (1) reduced rainfall, (2) increased evapotranspiration, (3) a high condensation temperature under warmer climate, (4) replacement of C_3 grasses by C_4 grasses, (5) downslope movements of vegetation belts, or (6) a change toward a ^{2}H-enriched moisture source (Collins et al., 2013; Dansgaard, 1964; Herrmann et al., 2017; Hou et al., 2008; Jaeschke et al., 2018; Kahmen et al., 2013a, 2013b; Risi et al., 2008; Rozanski et al., 1993; Sachse et al., 2012; Tipple and Pagani, 2010).

In the Govone section, $\delta^2H_{n\text{-alk}}$ values show a cyclic pattern in phase with lithological cyclicity (with more negative $\delta^2H_{n\text{-alk}}$ values in shales) and other paleoclimatic proxies such as element/Al ratios and *n*-alkane contents (Fig. 3). Such a pattern suggests that δ^2H variability was influenced by climate change at precession scale. Because $\delta^{13}C_{n\text{-alk}}$ values indicate persistent C_3 plant dominance, a change of vegetation can be excluded. Similarly, downslope and upslope vegetation shifts are unlikely to have caused such oscillations, although some minor effects cannot be excluded. In fact, to produce the observed differences in $\delta^2H_{n\text{-alk}}$ values between precession maxima and minima, altitudinal shifts of about 1000 m are needed; for modern environments gradients of 15-20‰/1000 m have been reported (Jaeschke et al., 2018 and references therein). In the modern and Messinian alpine environments, characterized by strong vegetation zonation, it is unlikely that shifts of such high magnitude may have occurred without a change in C_3 vegetation (e.g. conifer expansion). Such a severe shift is not recorded in the Govone data set. Therefore, the main cause of $\delta^2H_{n\text{-alk}}$ fluctuations must have been climate change driven by precession, including changes in (1) the amount and intensity of rainfall, (2) evapotranspiration, (3) temperature, and (4) relative moisture sources.

In the present-day northern Mediterranean south of the Alps, moisture is mainly sourced from the Western Mediterranean, the North Atlantic and, to a lesser extent, from Central Europe (e.g. Celle-Jeanton et al., 2001; Drumond et al., 2011; Gõmez-Hernández et al., 2013; Sodemann and Zubler, 2010). The resulting precipitation is typified by mixed δ^2H signatures, with the North

Atlantic supplying ^{2}H-depleted rainfall compared to the Mediterranean. Unfortunately, no data are available for moisture sourced from central Europe (Celle-Jeanton et al., 2001). Interestingly, climate models indicate that at least until the Pleistocene, the Western and northern Mediterranean were affected by precession-driven changes in the intensity of the Mediterranean storm track (Kutzbach et al., 2014; Toucanne et al., 2015). The Mediterranean storm track is related to the extension of North Atlantic depressions toward the Mediterranean, bringing additional precipitation from the North Atlantic during insolation maxima (Meijer and Tuenter, 2007; Toucanne et al., 2015).

Assuming similar moisture sources for the northern Mediterranean during the Late Messinian and considering that the Piedmont Basin was influenced by precession-controlled climate oscillations (Natalicchio et al., 2019), we suggest that the lower $\delta^{2}H_{n\text{-alk}}$ values in shales reflect a higher contribution of moisture from the North Atlantic during insolation maxima when the Mediterranean storm track was more intense (Fig. 5A). The resulting increased rainfall and lower evapotranspiration contributed to ^{2}H-depletion of long chain *n*-alkanes. As insolation maxima are expected to coincide with higher temperatures, the temperature effect cannot explain our observations. Conversely, the higher $\delta^{2}H_{n\text{-alk}}$ values in marls would indicate a weakening of the Mediterranean storm track at insolation minima (cf. Kutzbach et al., 2014; Toucanne et al., 2015), resulting in (1) relatively increased ^{2}H-enriched moisture from Mediterranean sources, (2) decreased precipitation, and (3) higher evapotranspiration rates (Fig. 5B). Expected lower temperatures had apparently not a major effect on the ^{2}H isotope patterns.

The increase of $\delta^{2}H_{n\text{-alk}}$ values across the MSC onset is mostly due to higher values in shales. Such a pattern would suggest an overall shift towards more arid conditions at first glance. However, this interpretation would be in conflict with the other proxies (lower element/Al ratios, increased contents of long chain *n*-alkanes, their lower CPI and lower δ^{13}C-values) and the paleovegetation reconstructions for the northern Mediterranean (e.g. Bertini and Martinetto, 2011), all pointing to an increase of humidity after the MSC onset. We consequently put forward the scenario that the observed ^{2}H-enrichment was caused by a progressively increasing moisture contribution from the Mediterranean. The observed increase of $\delta^2H_{n\text{-alk}}$ values coincided with a reduction of the Atlantic-Mediterranean connection at the onset of the MSC (cf. Flecker et al., 2015; Krijgsman et al., 2018; Roveri et al., 2014). Indeed, climate simulations for the Mediterranean area in the Late Miocene predict that the net hydrological budget, especially in the Western Mediterranean, was smaller than today because of basin restriction (Gladstone et al., 2007; Marzocchi et al., 2016; Meijer and Tuenter, 2007; Simon et al., 2017). It is consequently likely that evaporation was enhanced, resulting in an increased supply of ^{2}H-rich moisture from the Mediterranean (Fig. 5C). Due to these changes (1) ^{2}H became enriched in Mediterranean seawater (2) as well as in Mediterranean-derived moisture, and (3) Mediterranean-sourced (^{2}H-enriched) precipitation increased, causing an increase of humidity in the northern Mediterranean across the onset of the MSC.

6 Conclusions

The distribution of major elements and plant-wax derived long chain *n*-alkanes, as well as their $\delta^{13}C_{n\text{-alk}}$ and $\delta^2H_{n\text{-alk}}$ values, allowed tracing climate variability and hydrological changes in the northern Mediterranean basin across the onset of the Messinian salinity crisis (MSC). In the studied Govone section, fluctuations of major and trace elements (Ti/Al, Si/Al, Zr/Al ratios) and of long chain *n*-alkane contents are in phase with lithological cyclicity, confirming the control of precession-paced climate change on the deposition of pre-MSC and MSC strata. The observed cyclic pattern is mirrored by the δ^2H values of long chain *n*-alkanes, indicating the same precession-controlled driving forces had induced hydrological change. Shales, characterized by lower element/Al ratios and lower $\delta^2H_{n\text{-alk}}$ values as well as higher long chain *n*-alkane contents, were deposited under more humid conditions and higher riverine runoff at precession minima. Moister climate was favored by an intensified Mediterranean storm track, supplying ^{2}H-depleted moisture from the North Atlantic. Conversely, marls with their higher element/Al ratios, higher $\delta^2H_{n\text{-alk}}$ values, and lower long chain *n*-alkane contents reflect drier climate and reduced continental input at precession maxima and times of a weakened Mediterranean storm track. The $\delta^{13}C_{n\text{-alk}}$ values indicate that C_3 plants were the dominant source of terrestrial organic matter, agreeing with a persistently humid climate in the northern Mediterranean. Moreover, an increase of humidity, which is superimposed on the precession-controlled climate fluctuations, is inferred for the early phase of the MSC in the study area. This shift most likely reflects a hydrological change in the Mediterranean triggered by further restriction of the Atlantic-Mediterranean connection, which enhanced evaporation of Mediterranean seawater. Such evaporation produced ^{2}H-enriched moisture, which led to progressively ^{2}H-enriched precipitation in the study area after the onset of the MSC.

Acknowledgments

We thank S. Beckmann (Universität Hamburg) for technical support during organic geochemical analyses, E. Gründken and C. Lehners (Universität Oldenburg) for XRF analysis, J. Richarz (Universität Hamburg) for the analysis of TOC contents, R. Gennari (University of Turin) for help with the age model, and N. Burdanowitz (Universität Hamburg) for support in the application of molecular proxies. This project has received funding from the European Union’s Horizon 2020 research and innovation program under the Marie Skłodowska-Curie grant agreement No. 658252 to M. Natalicchio and from University of Torino grant to F. Dela Pierre. M. Sabino was funded by a doctoral scholarship provided by the Landesgraduiertenförderung of the state of Hamburg. E. Schefuß is funded and the hydrogen isotope analyses are supported by MARUM – Centre for Marine Environmental Sciences, University of Bremen. The article is further based upon work from COST Action “Uncovering the Mediterranean salt giant” (MEDSALT) supported by COST (European Cooperation in Science and Technology). Insightful comments of two anonymous reviewers helped improve the manuscript.

References

Aichner, B., Ott, F., Slowínski, M., Norýskiewicz, A.M., Brauer, A., Sachse, D., 2018. Leaf wax *n*-

alkane distributions record ecological changes during the Younger Dryas at Trzechowskie paleolake (northern Poland) without temporal delay. Clim. Past 14, 1607–1624. https://doi.org/10.5194/cp-14-1607-2018

Andersen, N., Paul, H.A., Bernasconi, S.M., McKenzie, J.A., Pasteur, L., Albrecht, P., 2001. Large and rapid climate variability during the Messinian salinity crisis: Evidence from deuterium concentrations of individual biomarkers. Geology 29, 799–802.

Badaut, D., Risacher, F., 1983. Authigenic smectite on diatom frustules in Bolivian saline lakes. Geochim. Cosmochim. Acta 47, 363–375. https://doi.org/10.1016/0016-7037(83)90259-4

Bellanca, A., Caruso, A., Ferruzza, G., Neri, R., Rouchy, J.M., Sprovieri, M., Blanc-Valleron, M.M., 2001. Transition from marine to hypersaline conditions in the Messinian Tripoli Formation from the marginal areas of the central Sicilian Basin. Sediment. Geol. 140, 87–105. https://doi.org/10.1016/S0037-0738(00)00173-1

Bernardi, E., 2013. Integrated stratigraphy of the northernmost record of the Messinian salinity crisis: new insights from the Tertiary Piedmont Basin. PhD thesis, University of Torino.

Bernardi, E., Dela Pierre, F., Gennari, R., Lozar, F., Violanti, D., 2012. Astrochronological calibration and paleoenvironmental reconstruction of the Messinian events at the Northern edge of the Mediterranean: The Govone section (Tertiary Piedmont Basin). Rend. Online Soc. Geol. Ital. 20, 10–11.

Bertini, A., 2006. The Northern Apennines palynological record as a contribute for the reconstruction of the Messinian palaeoenvironments. Sediment. Geol. 188–189, 235–258. https://doi.org/10.1016/j.sedgeo.2006.03.007

Bertini, A., Londeix, L., Maniscalco, R., Stefano, A. Di, Suc, J.-P., Clauzon, G., Gautier, F.F., Grasso, M., Gautier, F.F., 2006. Paleobiological evidence of depositional conditions in the Salt Member, Gessoso-Solfifera Formation (Messinian, Upper Miocene) of Sicily. Micropaleontology 44, 413. https://doi.org/10.2307/1486042

Bertini, A., Martinetto, E., 2011. Reconstruction of vegetation transects for the Messinian-

Piacenzian of Italy by means of comparative analysis of pollen, leaf and carpological records. Palaeogeogr. Palaeoclimatol. Palaeoecol. 304, 230–246. https://doi.org/10.1016/j.palaeo.2010.09.005

Bertini, A., Martinetto, E., 2008. Messinian to Zanclean vegetation and climate of Northern and Central Italy. Boll. della Soc. Paleontol. Ital. 47, 105–121. http://hdl.handle.net/2318/57252

Bigi, G., Cosentino, D., Parotto, M., Sartori, R., Scandone, P., 1990. Structural model Italy: Geodinamic Project. Consiglio Nazionale delle Ricerche (S.EL.CA, scale 1:500000, sheet 1).

Birgel, D., Thiel, V., Hinrichs, K.-U., Elvert, M., Campbell, K.A., Reitner, J., Farmer, J.D., Peckmann, J., 2006. Lipid biomarker patterns of methane-seep microbialites from the Mesozoic convergent margin of California. Org. Geochem. 37, 1289–1302. https://doi.org/10.1016/j.orggeochem.2006.02.004

Blanc-Valleron, M.M., Pierre, C., Caulet, J.P., Caruso, A., Rouchy, J.M., Cespuglio, G., Sprovieri, R., Pestrea, S., Di Stefano, E., 2002. Sedimentary, stable isotope and micropaleontological records of paleoceanographic change in the Messinian Tripoli Formation (Sicily, Italy). Palaeogeogr. Palaeoclimatol. Palaeoecol. 185, 255–286. https://doi.org/10.1016/S0031-0182(02)00302-4

Bray, E.E., Evans, E.D., 1961. Distribution of *n*-paraffins as a clue to recognition of source beds. Geochim. Cosmochim. Acta 22, 2–15. https://doi.org/10.1016/0016-7037(61)90069-2

Calvert, S.E., Fontugne, M.R., 2001. On the late Pleistocene-Holocene sapropel record of climatic and oceanographic variability in the Eastern Mediterranean. Paleoceanography 16, 78–94. https://doi.org/10.1029/1999PA000488

Calvert, S.E., Pedersen, T.F., 2007. Elemental Proxies for Palaeoclimatic and Palaeoceanographic Variability in Marine Sediments: Interpretation and Application, in: Hillaire-Marcel, C., De Vernal, A. (Eds.), Proxies in Late Cenozoic Paleoceanography, Developments in Marine Geology. Elsevier, pp. 567–644. https://doi.org/10.1016/S1572-5480(07)01019-6

Celle-Jeanton, H., Travi, Y., Blavoux, B., 2001. Isotopic typology of the precipitation in the

Western Mediterrenean region at the three different time scales. Geophys. Res. Lett. 28, 1215–1218. https://doi.org/10.1029/2000GL012407

Cerling, T.E., Harris, J.M., MacFadden, B.J., Leakey, M.G., Quade, J., Eisenmann, V., Ehleringer, J.R., 1997. Global vegetation change through the Miocene/Pliocene boundary. Nature 389, 153–158. https://doi.org/10.1038/38229

Cita, M.B., Wright, R.C., Ryan, W.B.F., Longinelli, A., 1978. Messinian Paleoenvironments. Initial Reports Deep Sea Drill. Proj. 42 Pt. 1 42, 1003–1035. https://doi.org/10.2973/dsdp.proc.42-1.153.1978

Collins, J.A., Schefuß, E., Mulitza, S., Prange, M., Werner, M., Tharammal, T., Paul, A., Wefer, G., 2013. Estimating the hydrogen isotopic composition of past precipitation using leaf-waxes from western Africa. Quat. Sci. Rev. 65, 88–101. https://doi.org/10.1016/j.quascirev.2013.01.007

Collister, J.W., Rieley, G., Stern, B., Eglinton, G., Fry, B., 1994. Compound-specific $\delta^{13}C$ analyses of leaf lipids from plants with differing carbon dioxide metabolisms. Org. Geochem. 21, 619–627. https://doi.org/10.1016/0146-6380(94)90008-6

Cortina, A., Grimalt, J.O., Rigual-Hernández, A., Ballegeer, A.M., Martrat, B., Sierro, F.J., Flores, J.A., 2016. The impact of ice-sheet dynamics in western Mediterranean environmental conditions during Terminations. An approach based on terrestrial long chain *n*-alkanes deposited in the upper slope of the Gulf of Lions. Chem. Geol. 430, 21–33. https://doi.org/10.1016/j.chemgeo.2016.03.015

Dansgaard, W., 1964. Stable isotopes in precipitation. Tellus 16, 436–468. https://doi.org/10.3402/tellusa.v16i4.8993

Dela Pierre, F., Bernardi, E., Cavagna, S., Clari, P., Gennari, R., Irace, A., Lozar, F., Lugli, S., Manzi, V., Natalicchio, M., Roveri, M., Violanti, D., 2011. The record of the Messinian salinity crisis in the Tertiary Piedmont Basin (NW Italy): The Alba section revisited. Palaeogeogr. Palaeoclimatol. Palaeoecol. 310, 238–255.

https://doi.org/10.1016/j.palaeo.2011.07.017

Dela Pierre, F., Festa, A., Irace, A., 2007. Interaction of tectonic, sedimentary, and diapiric processes in the origin of chaotic sediments: An example from the Messinian of Torino Hill (Tertiary Piedmont Basin, northwestern Italy). Bull. Geol. Soc. Am. 119, 1107–1119. https://doi.org/10.1130/B26072.1

Dela Pierre, F., Natalicchio, M., Lozar, F., Bonetto, S., Carnevale, G., Cavagna, S., Colombero, S., Sabino, M., Violanti, D., 2016. The northernmost record of the Messinian salinity crisis (Piedmont basin, Italy). Geol. F. Trips 8, 1–58. https://doi.org/10.3301/GFT.2016.03

Diefendorf, A.F., Freeman, K.H., Wing, S.L., Graham, H. V., 2011. Production of *n*-alkyl lipids in living plants and implications for the geologic past. Geochim. Cosmochim. Acta 75, 7472–7485. https://doi.org/10.1016/j.gca.2011.09.028

Diefendorf, A.F., Leslie, A.B., Wing, S.L., 2015. Leaf wax composition and carbon isotopes vary among major conifer groups. Geochim. Cosmochim. Acta 170, 145–156. https://doi.org/10.1016/j.gca.2015.08.018

Diefendorf, A.F., Freimuth, E.J., 2017. Extracting the most from terrestrial plant-derived *n*-alkyl lipids and their carbon isotopes from the sedimentary record: A review. Org. Geochem. 103, 1–21. https://doi.org/10.1016/j.orggeochem.2016.10.016

Drumond, A., Nieto, R., Hernandez, E., Gimeno, L., 2011. A Lagrangian analysis of the variation in moisture sources related to drier and wetter conditions in regions around the Mediterranean Basin. Nat. Hazards Earth Syst. Sci. 11, 2307–2320. https://doi.org/10.5194/nhess-11-2307-2011

Eglinton, G., Hamilton, R.J., 1967. Leaf epicuticular waxes. Science. 156, 1322–1335. https://doi.org/10.1126/science.156.3780.1322

Eglinton, T.I., Benitez-Nelson, B.C., Pearson, A., McNichol, A.P., Bauer, J.E., Druffel, E.R.M., 1997. Variability in radiocarbon ages of individual organic compounds from marine sediments. Science 277, 796–799. https://doi.org/10.1126/science.277.5327.796

Eglinton, T.I., Eglinton, G., 2008. Molecular proxies for paleoclimatology. Earth Planet. Sci. Lett. 275, 1–16. https://doi.org/10.1016/j.epsl.2008.07.012

Fauquette, S., Suc, J.P., Bertini, A., Popescu, S.M., Warny, S., Bachiri Taoufiq, N., Perez Villa, M.J., Chikhi, H., Feddi, N., Subally, D., Clauzon, G., Ferrier, J., 2006. How much did climate force the Messinian salinity crisis? Quantified climatic conditions from pollen records in the Mediterranean region. Palaeogeogr. Palaeoclimatol. Palaeoecol. 238, 281–301. https://doi.org/10.1016/j.palaeo.2006.03.029

Favre, E., François, L., Frédéric, F., Cheddadi, R., Lysiane, T., Jean-Pierre, S., 2007. Messinian vegetation maps of the Mediterranean region using models and interpolated pollen data. Geobios 40, 433–443. https://doi.org/10.1016/j.geobios.2006.12.002

Flecker, R., Krijgsman, W., Capella, W., de Castro Martíns, C., Dmitrieva, E., Mayser, J.P., Marzocchi, A., Modestu, S., Ochoa, D., Simon, D., Tulbure, M., van den Berg, B., van der Schee, M., de Lange, G., Ellam, R., Govers, R., Gutjahr, M., Hilgen, F., Kouwenhoven, T., Lofi, J., Meijer, P., Sierro, F.J., Bachiri, N., Barhoun, N., Alami, A.C., Chacon, B., Flores, J.A., Gregory, J., Howard, J., Lunt, D., Ochoa, M., Pancost, R., Vincent, S., Yousfi, M.Z., 2015. Evolution of the Late Miocene Mediterranean-Atlantic gateways and their impact on regional and global environmental change. Earth-Science Rev. 150, 365–392. https://doi.org/10.1016/j.earscirev.2015.08.007

Gennari, R., Lozar, F., Turco, E., Dela Pierre, F., Lugli, S., Manzi, V., Natalicchio, M., Roveri, M., Schreiber, B.C., Taviani, M., 2018. Integrated stratigraphy and paleoceanographic evolution of the pre-evaporitic phase of the Messinian salinity crisis in the Eastern Mediterranean as recorded in the Tokhni section (Cyprus island). Newsletters Stratigr. 51, 33–55. https://doi.org/10.1127/nos/2017/0350

Gladstone, R., Flecker, R., Valdes, P., Lunt, D., Markwick, P., 2007. The Mediterranean hydrologic budget from a Late Miocene global climate simulation. Palaeogeogr. Palaeoclimatol. Palaeoecol. 251, 254–267. https://doi.org/10.1016/j.palaeo.2007.03.050

Gõmez-Hernández, M., Drumond, A., Gimeno, L., Garcia-Herrera, R., 2013. Variability of moisture sources in the Mediterranean region during the period 1980-2000. Water Resour. Res. 49, 6781–6794. https://doi.org/10.1002/wrcr.20538

Herbert, T.D., Lawrence, K.T., Tzanova, A., Peterson, L.C., Caballero-Gill, R., Kelly, C.S., 2016. Late Miocene global cooling and the rise of modern ecosystems. Nat. Geosci. 9, 843–847. https://doi.org/10.1038/ngeo2813

Herrmann, N., Boom, A., Carr, A.S., Chase, B.M., West, A.G., Zabel, M., Schefuß, E., 2017. Hydrogen isotope fractionation of leaf wax *n*-alkanes in southern African soils. Org. Geochem. 109, 1–13. https://doi.org/10.1016/j.orggeochem.2017.03.008

Hilgen, F.J., Krijgsman, W., 1999. Cyclostratigraphy and astrochronology of the Tripoli diatomite formation (pre-evaporite Messinian, Sicily, Italy). Terra Nov. 11, 16–22. https://doi.org/10.1046/j.1365-3121.1999.00221.x

Hötzel, S., Dupont, L., Schefuß, E., Rommerskirchen, F., Wefer, G., 2013. The role of fire in Miocene to Pliocene C_4 grassland and ecosystem evolution. Nat. Geosci. 6, 1027–1030. https://doi.org/10.1038/ngeo1984

Hou, J., D’Andrea, W.J., Huang, Y., 2008. Can sedimentary leaf waxes record D/H ratios of continental precipitation? Field, model, and experimental assessments. Geochim. Cosmochim. Acta 72, 3503–3517. https://doi.org/10.1016/j.gca.2008.04.030

Hsü, K.J., Ryan, W.B.F., Cita, M.B., 1973. Late Miocene desiccation of the Mediterranean. Nature 242, 240–244. https://doi.org/10.1038/242240a0

Irace, A., Dela Pierre, F., Clari, P., 2005. “Normal” and “chaotic” deposits in the Messinian Gessoso-solfifera Fm. at the north eastern border of the Langhe domain (Tertiary Piedmont basin). Boll. Soc. Geol. Ital. 4, 77–85.

Jaeschke, A., Rethemeyer, J., Lappé, M., Schouten, S., Boeckx, P., Schefuß, E., 2018. Influence of land use on distribution of soil *n*-alkane δD and brGDGTs along an altitudinal transect in Ethiopia: Implications for (paleo)environmental studies. Org. Geochem. 124, 77–87.

https://doi.org/10.1016/j.orggeochem.2018.06.006

Jiménez-Moreno, G., Fauquette, S., Suc, J.P., 2010. Miocene to Pliocene vegetation reconstruction and climate estimates in the Iberian Peninsula from pollen data. Rev. Palaeobot. Palynol. 162, 403–415. https://doi.org/10.1016/j.revpalbo.2009.08.001

Jiménez-Moreno, G., Pérez-Asensio, J.N., Larrasoaña, J.C., Aguirre, J., Civis, J., Rivas-Carballo, M.R., Valle-Hernández, M.F., González-Delgado, J.A., 2013. Vegetation, sea-level, and climate changes during the Messinian salinity crisis. Bull. Geol. Soc. Am. 125, 432–444. https://doi.org/10.1130/B30663.1

Kahmen, A., Hoffmann, B., Schefuß, E., Arndt, S.K., Cernusak, L.A., West, J.B., Sachse, D., 2013a. Leaf water deuterium enrichment shapes leaf wax *n*-alkane δD values of angiosperm plants II: Observational evidence and global implications. Geochim. Cosmochim. Acta 111, 50–63. https://doi.org/10.1016/j.gca.2012.09.004

Kahmen, A., Schefuß, E., Sachse, D., 2013b. Leaf water deuterium enrichment shapes leaf wax *n*-alkane δD values of angiosperm plants I: Experimental evidence and mechanistic insights. Geochim. Cosmochim. Acta 111, 39–49. https://doi.org/10.1016/j.gca.2012.09.003

Kouwenhoven, T.J., Morigi, C., Negri, A., Giunta, S., Krijgsman, W., Rouchy, J.M., 2006. Paleoenvironmental evolution of the eastern Mediterranean during the Messinian: Constraints from integrated microfossil data of the Pissouri Basin (Cyprus). Mar. Micropaleontol. 60, 17–44. https://doi.org/10.1016/j.marmicro.2006.02.005

Krijgsman, W., Capella, W., Simon, D., Hilgen, F.J., Kouwenhoven, T.J., Meijer, P.T., Sierro, F.J., Tulbure, M.A., van den Berg, B.C.J., van der Schee, M., Flecker, R., 2018. The Gibraltar Corridor: Watergate of the Messinian Salinity Crisis. Mar. Geol. 403, 238–246. https://doi.org/10.1016/j.margeo.2018.06.008

Krijgsman, W., Hilgen, F.J., Raffi, I., Sierro, F.J., Wilson, D.S., 1999. Chronology, causes and progression of the Messinian salinity crisis. Nature 400, 652–655. https://doi.org/10.1038/23231

Kutzbach, J.E., Chen, G., Cheng, H., Edwards, R.L., Liu, Z., 2014. Potential role of winter rainfall in explaining increased moisture in the Mediterranean and Middle East during periods of maximum orbitally-forced insolation seasonality. Clim. Dyn. 42, 1079–1095. https://doi.org/10.1007/s00382-013-1692-1

Laskar, J., Robutel, P., Joutel, F., Gastineau, M., Correia, A.C.M., Levrard, B., 2004. A long-term numerical solution for the insolation quantities of the Earth. Astron. Astrophys. 428, 261–285. https://doi.org/10.1051/0004-6361:20041335

Lozar, F., Negri, A., 2019. A review of basin-wide calcareous nannofossil bioevents in the Mediterranean at the onset of the Messinian salinity crisis. Mar. Micropaleontol. 101752. https://doi.org/10.1016/J.MARMICRO.2019.101752

Lozar, F., Violanti, D., Bernardi, E., Dela Pierre, F., Natalicchio, M., 2018. Identifying the onset of the Messinian salinity crisis: A reassessment of the biochronostratigraphic tools (Piedmont Basin, NW Italy). Newsletters Stratigr. 51, 11–31. https://doi.org/10.1127/nos/2017/0354

Lugli, S., Manzi, V., Roveri, M. and Schreiber, C. B., 2010. The Primary Lower Gypsum in the Mediterranean: a new facies interpretation for the first stage of the Messinian salinity crisis. Palaeogeogr. Palaeoclimatol. Palaeoecol. 297, 83–99. http://dx.doi.org/10.1016/j.palaeo.2010.07.017

Luo, P., Peng, P.A., Lü, H.Y., Zheng, Z., Wang, X., 2012. Latitudinal variations of CPI values of long-chain *n*-alkanes in surface soils: Evidence for CPI as a proxy of aridity. Sci. China Earth Sci. 55, 1134–1146. https://doi.org/10.1007/s11430-012-4401-8

Madhavan, S., Treichel, I., O'Leary, M.H., 1991. Effects of relative humidity on carbon isotope fractionation in plants. Bot. Acta. https://doi.org/10.1111/j.1438-8677.1991.tb00232.x

Manzi, V., Gennari, R., Hilgen, F., Krijgsman, W., Lugli, S., Roveri, M., Sierro, F.J., 2013. Age refinement of the Messinian salinity crisis onset in the Mediterranean. Terra Nov. 25, 315–322. https://doi.org/10.1111/ter.12038

Manzi, V., Roveri, M., Gennari, R., Bertini, A., Biffi, U., Giunta, S., Iaccarino, S.M., Lanci, L., Lugli, S., Negri, A., Riva, A., Rossi, M.E., Taviani, M., 2007. The deep-water counterpart of the Messinian Lower Evaporites in the Apennine foredeep: The Fanantello section (Northern Apennines, Italy). Palaeogeogr. Palaeoclimatol. Palaeoecol. 251, 470–499. https://doi.org/10.1016/j.palaeo.2007.04.012

Martinez-Ruiz, F., Kastner, M., Gallego-Torres, D., Rodrigo-Gámiz, M., Nieto-Moreno, V., Ortega-Huertas, M., 2015. Paleoclimate and paleoceanography over the past 20,000 yr in the Mediterranean Sea Basins as indicated by sediment elemental proxies. Quat. Sci. Rev. 107, 25–46. https://doi.org/10.1016/j.quascirev.2014.09.018

Marzocchi, A., Flecker, R., van Baak, C.G.C., Lunt, D.J., Krijgsman, W., 2016. Mediterranean outflow pump: An alternative mechanism for the Lago-mare and the end of the Messinian Salinity Crisis. Geology 44, 523–526. https://doi.org/10.1130/G37646.1

Mayser, J.P., Flecker, R., Marzocchi, A., Kouwenhoven, T.J., Lunt, D.J., Pancost, R.D., 2017. Precession driven changes in terrestrial organic matter input to the Eastern Mediterranean leading up to the Messinian Salinity Crisis. Earth Planet. Sci. Lett. 462, 199–211. https://doi.org/10.1016/j.epsl.2017.01.029

Meijer, P.T., Tuenter, E., 2007. The effect of precession-induced changes in the Mediterranean freshwater budget on circulation at shallow and intermediate depth. J. Mar. Syst. 68, 349–365. https://doi.org/10.1016/j.jmarsys.2007.01.006

Moller, T., Schulz, H., Hamann, Y., Dellwig, O., Kucera, M., 2012. Sedimentology and geochemistry of an exceptionally preserved last interglacial sapropel S5 in the Levantine Basin (Mediterranean Sea). Mar. Geol. 291–294, 34–48. https://doi.org/10.1016/j.margeo.2011.10.011

Mosca, P., Polino, R., Rogledi, S., Rossi, M., 2010. New data for the kinematic interpretation of the Alps-Apennines junction (Northwestern Italy). Int. J. Earth Sci. 99, 833–849. https://doi.org/10.1007/s00531-009-0428-2

Naafs, B.D.A., Hefter, J., Acton, G., Haug, G.H., Martínez-Garcia, A., Pancost, R., Stein, R., 2012.

Strengthening of North American dust sources during the late Pliocene (2.7Ma). Earth Planet. Sci. Lett. 317–318, 8–19. https://doi.org/10.1016/j.epsl.2011.11.026

Natalicchio, M., Birgel, D., Peckmann, J., Lozar, F., Carnevale, G., Liu, X., Hinrichs, K.-U., Dela Pierre, F., 2017. An archaeal biomarker record of paleoenvironmental change across the onset of the Messinian salinity crisis in the absence of evaporites (Piedmont Basin, Italy). Org. Geochem. 113, 242–253. https://doi.org/10.1016/j.orggeochem.2017.08.014

Natalicchio, M., Dela Pierre, F., Birgel, D., Brumsack, H., Carnevale, G., Gennari, R., Gier, S., Lozar, F., Pellegrino, L., Sabino, M., Schnetger, B., Peckmann, J., 2019. Paleoenvironmental change in a precession-paced succession across the onset of the Messinian salinity crisis: Insight from element geochemistry and molecular fossils. Palaeogeogr. Palaeoclimatol. Palaeoecol. 518, 45–61. https://doi.org/10.1016/j.palaeo.2019.01.009

Pancost, R.D., Boot, C.S., 2004. The palaeoclimatic utility of terrestrial biomarkers in marine sediments. Mar. Chem. 92, 239–261. https://doi.org/10.1016/j.marchem.2004.06.029

Pedentchouk, N., Zhou, Y., 2018. Factors controlling carbon and hydrogen isotope fractionation during biosynthesis of lipids by phototrophic organisms, in: Hydrocarbons, Oils and Lipids: Diversity, Origin, Chemistry and Fate. Springer International Publishing, pp. 1–24. https://doi.org/10.1007/978-3-319-54529-5_37-1

Popov, S.V., Shcherba, I.G., Ilyina, L.B., Nevesskaya, L.A., Paramonova, N.P., Khondkarian, S.O., Magyar, I., 2006. Late Miocene to Pliocene palaeogeography of the Paratethys and its relation to the Mediterranean. Palaeogeogr. Palaeoclimatol. Palaeoecol. https://doi.org/10.1016/j.palaeo.2006.03.020

Pound, M.J., Haywood, A.M., Salzmann, U., Riding, J.B., 2012. Global vegetation dynamics and latitudinal temperature gradients during the Mid to Late Miocene (15.97-5.33 Ma). Earth-Science Rev. 112, 1–22. https://doi.org/10.1016/j.earscirev.2012.02.005

Risi, C., Bony, S., Vimeux, F., 2008. Influence of convective processes on the isotopic composition (δ^{18}O and δD) of precipitation and water vapor in the tropics: 2. Physical interpretation of the amount effect. J. Geophys. Res. Atmos. 113, 1–12. https://doi.org/10.1029/2008JD009943

Rossi, M., 2017. Outcrop and seismic expression of stratigraphic patterns driven by accommodation and sediment supply turnarounds: Implications on the meaning and variability of unconformities in syn-orogenic basins. Mar. Pet. Geol. 87, 112–127. https://doi.org/10.1016/j.marpetgeo.2017.03.032

Rossi, M., Craig, J., 2016. A new perspective on sequence stratigraphy of syn-orogenic basins: Insights from the Tertiary Piedmont Basin (Italy) and implications for play concepts and reservoir heterogeneity. Geol. Soc. Spec. Publ. 436, 93–133. https://doi.org/10.1144/SP436.10

Roveri, M., Flecker, R., Krijgsman, W., Lofi, J., Lugli, S., Manzi, V., Sierro, F.J., Bertini, A., Camerlenghi, A., De Lange, G., Govers, R., Hilgen, F.J., Hübscher, C., Meijer, P.T., Stoica, M., 2014. The Messinian Salinity Crisis: Past and future of a great challenge for marine sciences. Mar. Geol. 352, 25–58. https://doi.org/10.1016/j.margeo.2014.02.002

Roveri, M., Lugli, S., Manzi, V., Schreiber, B.C., 2008. The Messinian Sicilian stratigraphy revisited: New insights for the Messinian salinity crisis. Terra Nov. 20, 483–488. https://doi.org/10.1111/j.1365-3121.2008.00842.x

Rozanski, K., Araguás-Araguás, L., Gonfiantini, R., 1993. Isotopic patterns in modern global precipitation. Clim. Chang. Cont. Isot. Rec. 78, 1–36. https://doi.org/10.1029/gm078p0001

Sachse, D., Billault, I., Bowen, G.J., Chikaraishi, Y., Dawson, T.E., Feakins, S.J., Freeman, K.H., Magill, C.R., McInerney, F.A., van der Meer, M.T.J., Polissar, P., Robins, R.J., Sachs, J.P., Schmidt, H.-L., Sessions, A.L., White, J.W.C., West, J.B., Kahmen, A., 2012. Molecular paleohydrology: Interpreting the hydrogen-isotopic composition of lipid biomarkers from photosynthesizing organisms. Annu. Rev. Earth Planet. Sci. 40, 221–249. https://doi.org/10.1146/annurev-earth-042711-105535

Schefuß, E., Ratmeyer, V., Stuut, J.B.W., Jansen, J.H.F., Sinninghe Damsté, J.S., 2003. Carbon isotope analyses of *n*-alkanes in dust from the lower atmosphere over the central eastern Atlantic. Geochim. Cosmochim. Acta 67, 1757–1767. https://doi.org/10.1016/S0016-

7037(02)01414-X

Schefuß, E., Schouten, S., Schneider, R.R., 2005. Climatic controls on central African hydrology during the past 20,000 years. Nature 437, 1003–1006. https://doi.org/10.1038/nature03945

Schieber, J., 1996. Early diagenetic silica deposition in algal cysts and spores; a source of sand in black shales? J. Sediment. Petrol. 66, 175–183.

Schnetger, B., 1992. Chemical-composition of loess from a local and worldwide view. Neues Jahrb. Miner. Monatshefte 1, 29–47.

Schnetger, B., Brumsack, H.J., Schale, H., Hinrichs, J., Dittert, L., 2000. Geochemical characteristics of deep-sea sediments from the Arabian Sea: A high-resolution study. Deep. Res. Part II Top. Stud. Oceanogr. 47, 2735–2768. https://doi.org/10.1016/S0967-0645(00)00047-3

Sierro, F.J., Flores, J.A., Francés, G., Vazquez, A., Utrilla, R., Zamarreño, I., Erlenkeuser, H., Barcena, M.A., 2003. Orbitally-controlled oscillations in planktic communities and cyclic changes in western Mediterranean hydrography during the Messinian. Palaeogeogr. Palaeoclimatol. Palaeoecol. 190, 289–316. https://doi.org/10.1016/S0031-0182(02)00611-9

Sierro, F.J., Flores, J.A., Zamarreno, I., Vazquez, A., Utrilla, R., Frances, G., Hilgen, F.J., Krijgsman, W., 1999. Messinian pre-evaporite sapropels and procession-induced oscillations in western Mediterranean climate. Mar. Geol. 153, 137–146. https://doi.org/10.1016/S0025-3227(98)00085-1

Sierro, F.J., Hilgen, F.J., Krijgsman, W., Flores, J.A., 2001. The Abad composite (SE Spain): A Messinian reference section for the Mediterranean and the APTS. Palaeogeogr. Palaeoclimatol. Palaeoecol. 168, 141–169. https://doi.org/10.1016/S0031-0182(00)00253-4

Simon, D., Marzocchi, A., Flecker, R., Lunt, D.J., Hilgen, F.J., Meijer, P.T., 2017. Quantifying the Mediterranean freshwater budget throughout the late Miocene: New implications for sapropel formation and the Messinian Salinity Crisis. Earth Planet. Sci. Lett. 472, 25–37. https://doi.org/10.1016/j.epsl.2017.05.013

Sinninghe Damsté, J.S., Kuypers, M.M.M., Schouten, S., Schulte, S., Rullkötter, J., 2003. The lycopane/C_{31} *n*-alkane ratio as a proxy to assess palaeoxicity during sediment deposition. Earth Planet. Sci. Lett. 209, 215–226. https://doi.org/10.1016/S0012-821X(03)00066-9

Sodemann, H., Zubler, E., 2010. Seasonal and inter-annual variability of the moisture sources for alpine precipitation during 1995-2002. Int. J. Climatol. 30, 947–961. https://doi.org/10.1002/joc.1932

Strömberg, C.A.E., 2011. Evolution of grasses and grassland ecosystems. Annu. Rev. Earth Planet. Sci. 39, 517–544. https://doi.org/10.1146/annurev-earth-040809-152402

Sturani, C., 1976. Messinian facies in the Piedmont basin. Mem. Soc. Geol. Ital. 16, 11–25.

Sturani, C., 1973. A fossil eel (*Anguilla* sp.) from the Messinian of Alba (Tertiary Piedmont Basin). Palaeoenvironmental and palaeogeographic implications, in: Drooger, C.W. (Ed.), Messinian Events in the Mediterranean. K. Nederl. Akad. Wetensch. Amsterdam, pp. 243–255.

Suc, J.-P., Bessais, E., 1990. Pérennité d'un climat thermo-xérique en Sicile avant, pendant, après la crise de salinité messinienne. Comptes rendus l'Académie des Sci. Série 2, Mécanique, Phys. Chim. Sci. l'univers, Sci. la Terre 310, 1701–1707.

Tipple, B.J., Pagani, M., 2010. A 35Myr North American leaf-wax compound-specific carbon and hydrogen isotope record: Implications for C_4 grasslands and hydrologic cycle dynamics. Earth Planet. Sci. Lett. 299, 250–262. https://doi.org/10.1016/j.epsl.2010.09.006

Toucanne, S., Angue Minto'o, C.M., Fontanier, C., Bassetti, M.A., Jorry, S.J., Jouet, G., 2015. Tracking rainfall in the northern Mediterranean borderlands during sapropel deposition. Quat. Sci. Rev. 129, 178–195. https://doi.org/10.1016/j.quascirev.2015.10.016

Tribovillard, N., Algeo, T.J., Lyons, T., Riboulleau, A., 2006. Trace metals as paleoredox and paleoproductivity proxies: An update. Chem. Geol. 232, 12–32. https://doi.org/10.1016/j.chemgeo.2006.02.012

Tzanova, A., Herbert, T.D., Peterson, L., 2015. Cooling Mediterranean Sea surface temperatures during the Late Miocene provide a climate context for evolutionary transitions in Africa and

Eurasia. Earth Planet. Sci. Lett. 419, 71–80. https://doi.org/10.1016/j.epsl.2015.03.016

van der Laan, E., Hilgen, F.J., Lourens, L.J., de Kaenel, E., Gaboardi, S., Iaccarino, S., 2012. Astronomical forcing of Northwest African climate and glacial history during the late Messinian (6.5-5.5Ma). Palaeogeogr. Palaeoclimatol. Palaeoecol. 313, 107–126 https://doi.org/10.1016/j.palaeo.2011.10.013

Vasiliev, I., Karakitsios, V., Bouloubassi, I., Agiadi, K., Kontakiotis, G., Antonarakou, A., Triantaphyllou, M., Gogou, A., Kafousia, N., de Rafélis, M., Zarkogiannis, S., Kaczmar, F., Parinos, C., Pasadakis, N., 2019. Large sea surface temperature, salinity, and productivity preservation changes preceding the onset of the Messinian Salinity Crisis in the eastern Mediterranean Sea. Paleoceanogr. Paleoclimatology 34, 182–202. https://doi.org/10.1029/2018PA003438

Vasiliev, I., Mezger, E.M., Lugli, S., Reichart, G.J., Manzi, V., Roveri, M., 2017. How dry was the Mediterranean during the Messinian salinity crisis? Palaeogeogr. Palaeoclimatol. Palaeoecol. 471, 120–133. https://doi.org/10.1016/j.palaeo.2017.01.032

Vasiliev, I., Reichart, G.J., Grothe, A., Sinninghe Damsté, J.S., Krijgsman, W., Sangiorgi, F., Weijers, J.W.H., van Roij, L., 2015. Recurrent phases of drought in the upper Miocene of the Black Sea region. Palaeogeogr. Palaeoclimatol. Palaeoecol. 423, 18–31. https://doi.org/10.1016/j.palaeo.2015.01.020

Vasiliev, I., Reichart, G.J., Krijgsman, W., 2013. Impact of the Messinian Salinity Crisis on Black Sea hydrology-Insights from hydrogen isotopes analysis on biomarkers. Earth Planet. Sci. Lett. 362, 272–282 https://doi.org/10.1016/j.epsl.2012.11.038

Violanti, D., Lozar, F., Natalicchio, M., Dela Pierre, F., Bernardi, E., Clari, P., Cavagna, S., 2013. Stress-tolerant microfossils of a Messinian succession from the Northern Mediterranean basin (Pollenzo section, Piedmont, northwestern Italy). Boll. della Soc. Paleontol. Ital. 52, 45–54. https://doi.org/10.4435/BSPI.2013.09

Wakeham, G., Freeman, K.H., Pease, L.T.K., Hayes, J.M., 1993. A photoautotrophic source for lycopane in marine water columns 57, 159–165.

Wehausen, R., Brumsack, H.J., 2000. Chemical cycles in Pliocene sapropel-bearing and sapropel-barren eastern Mediterranean sediments. Palaeogeogr. Palaeoclimatol. Palaeoecol. 158, 325–352. https://doi.org/10.1016/S0031-0182(00)00057-2

Wehausen, R., Brumsack, H.J., 1999. Cyclic variations in the chemical composition of eastern Mediterranean Pliocene sediments: A key for understanding sapropel formation. Mar. Geol. 153, 161–176. https://doi.org/10.1016/S0025-3227(98)00083-8

Zachos, J., Pagani, H., Sloan, L., Thomas, E., Billups, K., 2001. Trends, rhythms, and aberrations in global climate 65 Ma to present. Science. 292, 686–693. https://doi.org/10.1126/science.1059412

Figure captions

Fig. 1. (A) Structural sketch map of the Piedmont Basin indicating the location of the Govone section (modified from Bigi et al., 1990). Insert in the top left corner: Piedmont Basin position (star) and distribution of the Messinian evaporites on the Italian peninsula and in the Western Mediterranean (modified from Natalicchio et al., 2019). Gray dotted lines indicate the isobaths of the base of the Pliocene. (B) Stratigraphic relationships among the Messinian deposits of the Piedmont Basin along a N-S profile, with the position of the Govone section (modified from Dela Pierre et al., 2011). (C) Overview of the Govone lithological cycles deposited across the Messinian salinity crisis onset (red line). The insets indicate the position of figures D and E. (D) Laminated pre-MSC shale. Note lamination. (E) Homogenous pre-MSC marl. MSC: Messinian salinity crisis; PLG: Primary Lower Gypsum unit

Fig. 2. (A) Govone section (Bernardi, 2103) tuned with astronomical solution (65° N summer insolation; Laskar et al., 2004) and correlated with the Perales section (Spain; Manzi et al., 2013; Sierro et al., 2001). (B) The investigated interval (cycles Gm26 – Gm33). FAO: first abundant occurrence; MSC: Messinian salinity crisis.

Fig. 3. From left to right of the Govone section: Si/Al, Ti/Al and Zr/Al ratios; sum of the odd-numbered C_{27}-C_{33} *n*-alkanes; Carbon Preference Index (CPI); compound-specific carbon ($\delta^{13}C_{n\text{-alk}}$) and hydrogen ($\delta^{2}H_{n\text{-alk}}$) stable isotope compositions. Error bars are indicated where measurements have been conducted at least in duplicate. Shaded pale green areas indicate shales. Ages reflecting the midpoint of shale layers (far left) are from Manzi et al. (2013).

Fig. 4. Partial GC-MS chromatograms (*m/z* 71) of sedimentary *n*-alkanes of two representative samples of shale (left) and marl (right). The *n*-C_{35} alkane coelutes with lycopane (Ly). Note the relative intensity of the internal standard (IS) compared to the *n*-alkanes, indicating the higher content of lipids in shales compared to marls.

Fig. 5. Paleoclimatic and paleohydrological reconstruction of the Piedmont Basin at precession minima/insolation maxima (A) and precession maxima/insolation minima (B) across the onset of the MSC. (C) Reconstruction of the northern Mediterranean hydrological pattern during the early MSC. Areas of major evaporation (according to Gladstone et al., 2007) are indicated in shades of blue. Green shaded area indicates the northern Mediterranean. Paleogeography modified from Popov et al. (2006). G: Govone section; MSC: Messinian salinity crisis; N. Atlantic: North Atlantic; W. Med.: Western Mediterranean.

Highlights

- Proxies indicate climate change driven by precession in the Northern Mediterranean
- C_3 vegetation dominated after the onset of the crisis at precession maxima
- Source areas of moisture varied as a function of precession
- Humidity increased after the onset of the Messinian salinity crisis

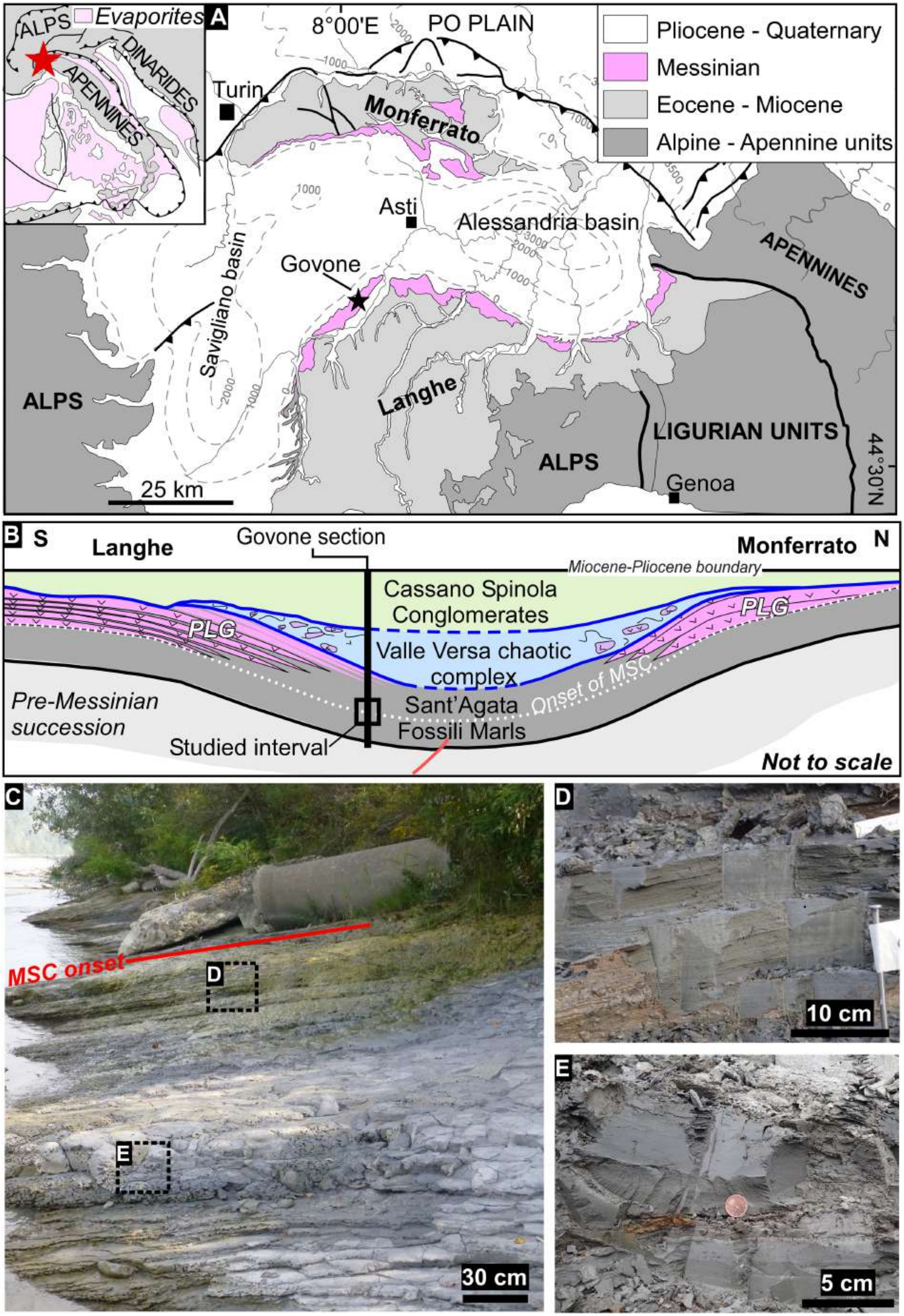
A
Evaporites
ALPS
DINARIDES
APENNINES
8°00'E
PO PLAIN
Pliocene - Quaternary
Messinian
Eocene - Miocene
Alpine - Apennine units
Turin
Monferrato
Asti
Alessandria basin
Govone
Savigliano basin
Langhe
ALPS
APENNINES
LIGURIAN UNITS
ALPS
Genoa
25 km
44°30'N
1000
2000
3000
0
B
S
Langhe
Govone section
Monferrato
N
Miocene-Pliocene boundary
Cassano Spinola Conglomerates
PLG
PLG
Valle Versa chaotic complex
Onset of MSC
Pre-Messinian succession
Sant'Agata Fossili Marls
Studied interval
Not to scale
C
MSC onset
D
E
30 cm
D
10 cm
E
5 cm

Figure 1

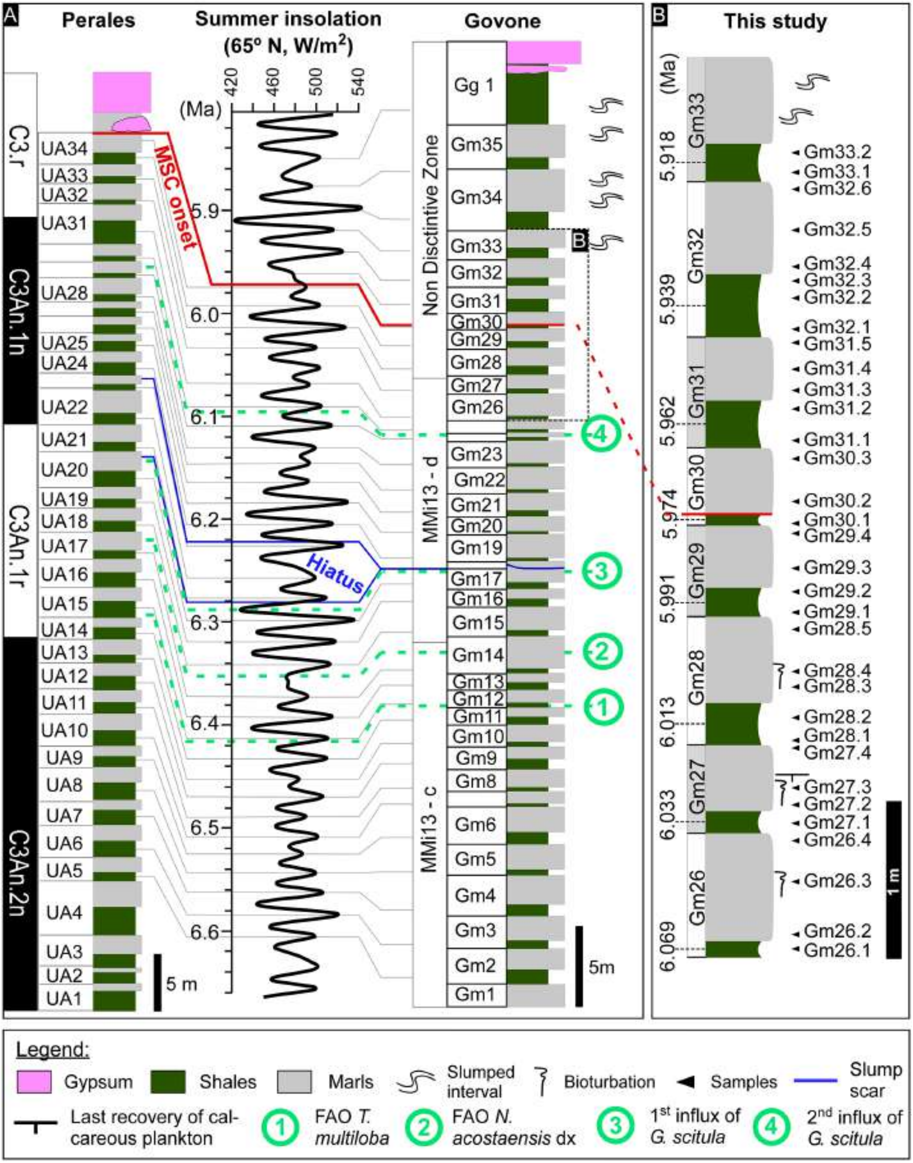
A
Perales
Summer insolation
(65° N, W/m2)
420
460
500
540
(Ma)
5.9
6.0
6.1
6.2
6.3
6.4
6.5
6.6
Govone
C3.r
C3An.1n
C3An.1r
C3An.2n
UA34
UA33
UA32
UA31
UA28
UA25
UA24
UA22
UA21
UA20
UA19
UA18
UA17
UA16
UA15
UA14
UA13
UA12
UA11
UA10
UA9
UA8
UA7
UA6
UA5
UA4
UA3
UA2
UA1
MSC onset
Hiatus
5 m
Non Disctintive Zone
MMi13 - d
MMi13 - c
Gg 1
Gm35
Gm34
Gm33
Gm32
Gm31
Gm30
Gm29
Gm28
Gm27
Gm26
Gm23
Gm22
Gm21
Gm20
Gm19
Gm17
Gm16
Gm15
Gm14
Gm13
Gm12
Gm11
Gm10
Gm9
Gm8
Gm6
Gm5
Gm4
Gm3
Gm2
Gm1
B
4
3
2
1
5m
B
This study
(Ma)
5.918
5.939
5.962
5.974
5.991
6.013
6.033
6.069
Gm33
Gm32
Gm31
Gm30
Gm29
Gm28
Gm27
Gm26
Gm33.2
Gm33.1
Gm32.6
Gm32.5
Gm32.4
Gm32.3
Gm32.2
Gm32.1
Gm31.5
Gm31.4
Gm31.3
Gm31.2
Gm31.1
Gm30.3
Gm30.2
Gm30.1
Gm29.4
Gm29.3
Gm29.2
Gm29.1
Gm28.5
Gm28.4
Gm28.3
Gm28.2
Gm28.1
Gm27.4
Gm27.3
Gm27.2
Gm27.1
Gm26.4
Gm26.3
Gm26.2
Gm26.1
1 m
Legend:
Gypsum
Shales
Marls
Slumped interval
Bioturbation
Samples
Slump scar
Last recovery of calcareous plankton
1 FAO T. multiloba
2 FAO N. acostaensis dx
3 1st influx of G. scitula
4 2nd influx of G. scitula

Figure 2

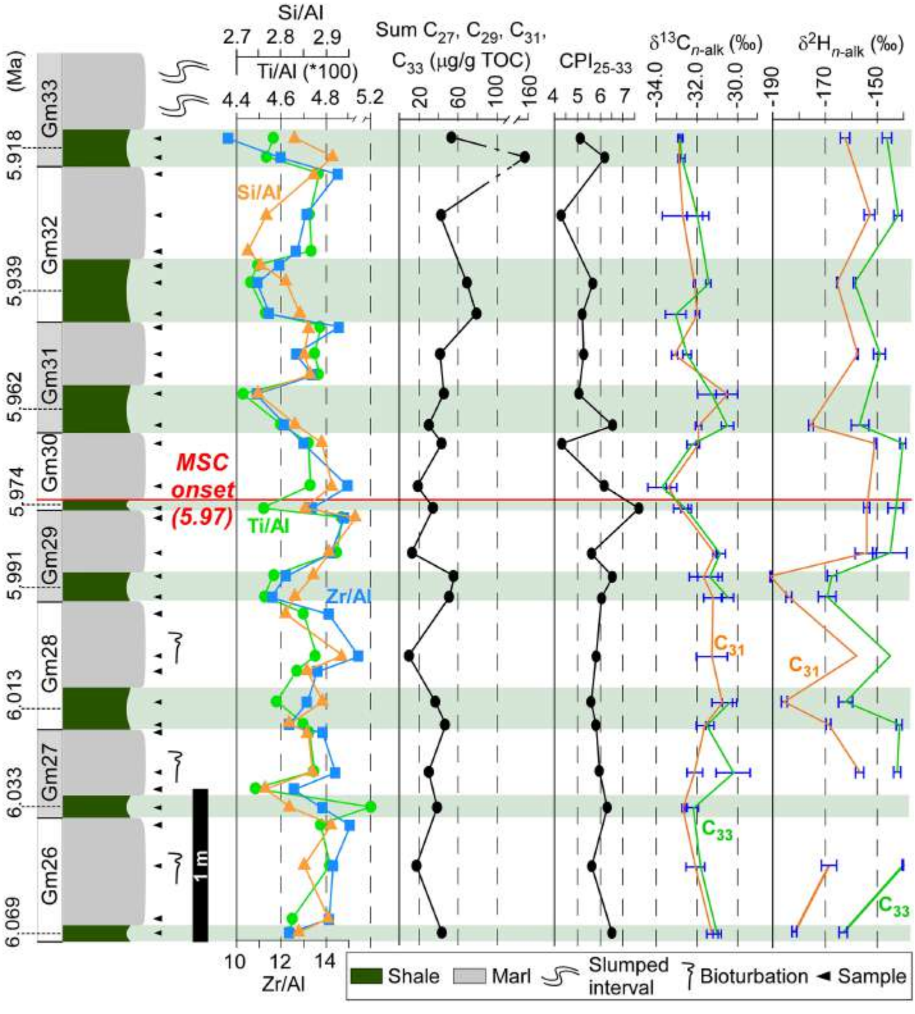
(Ma)
Gm33
5.918
Gm32
5.939
Gm31
5.962
Gm30
5.974
Gm29
5.991
Gm28
6.013
Gm27
6.033
Gm26
6.069
MSC onset (5.97)
1 m
Si/Al
2.7 2.8 2.9
Ti/Al (*100)
4.4 4.6 4.8 5.2
Si/Al
Ti/Al
Zr/Al
10 12 14
Zr/Al
Sum C_{27}, C_{29}, C_{31}, C_{33} (μg/g TOC)
20 60 100 160
CPI_{25-33}
4 5 6 7
$\delta^{13}C_{n\text{-alk}}$ (‰)
-34.0 -32.0 -30.0
C_{31}
C_{33}
$\delta^{2}H_{n\text{-alk}}$ (‰)
-190 -170 -150
C_{31}
C_{33}
Shale
Marl
Slumped interval
Bioturbation
Sample

Figure 3

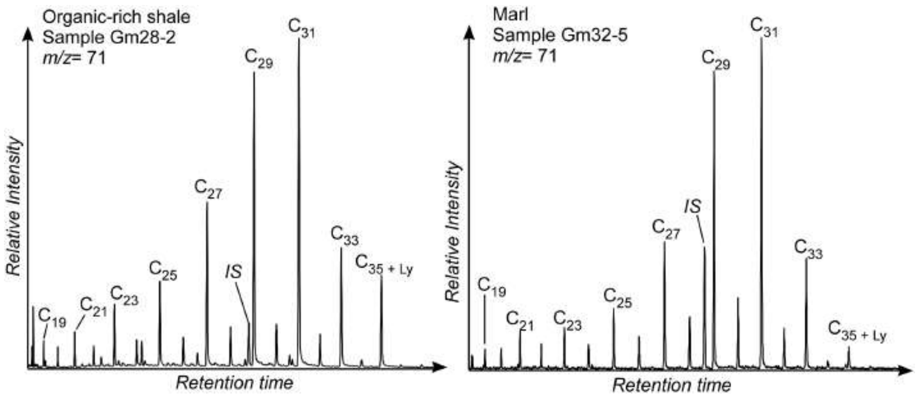
Organic-rich shale
Sample Gm28-2
m/z= 71
Relative Intensity
Retention time
C_{19}
C_{21}
C_{23}
C_{25}
C_{27}
IS
C_{29}
C_{31}
C_{33}
C_{35} + Ly
Marl
Sample Gm32-5
m/z= 71
Relative Intensity
Retention time
C_{19}
C_{21}
C_{23}
C_{25}
C_{27}
IS
C_{29}
C_{31}
C_{33}
C_{35} + Ly

Figure 4

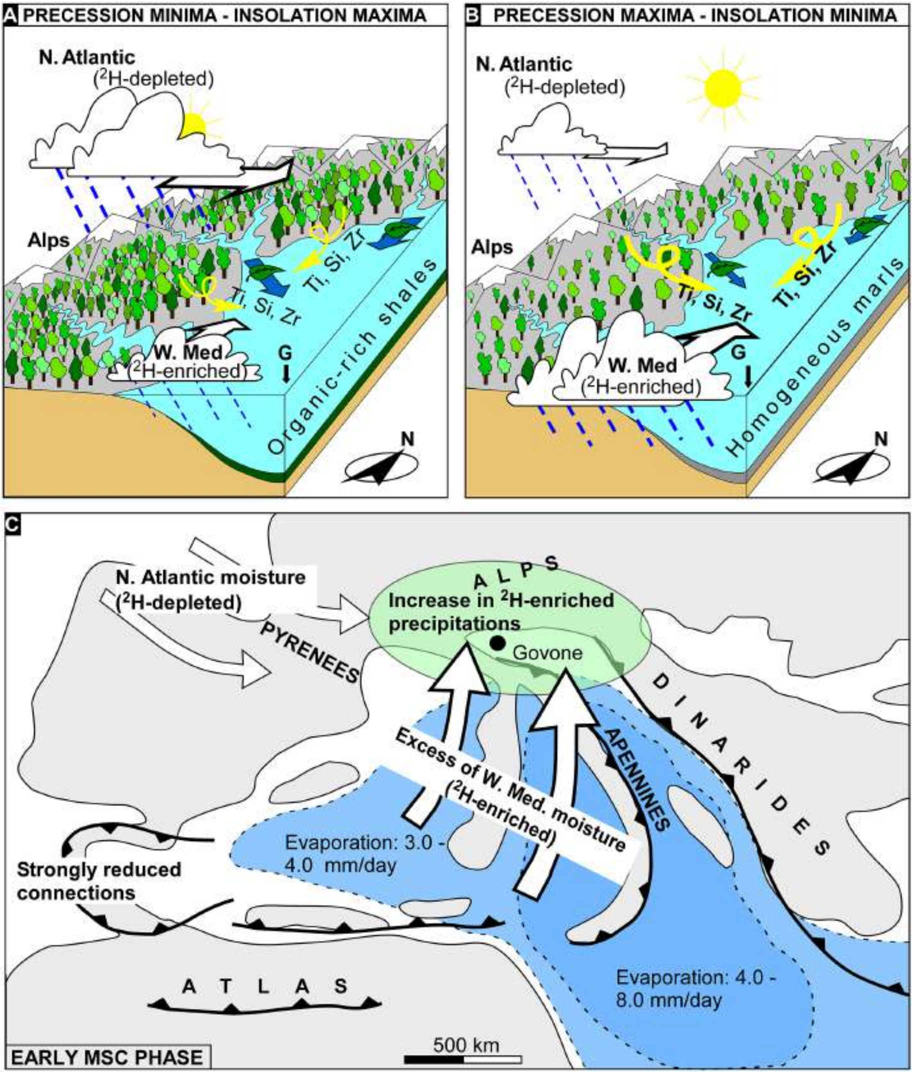
A PRECESSION MINIMA - INSOLATION MAXIMA
N. Atlantic
(^{2}H-depleted)
Alps
Ti, Si, Zr
Ti, Si, Zr
W. Med
(^{2}H-enriched)
G
Organic-rich shales
N
B PRECESSION MAXIMA - INSOLATION MINIMA
N. Atlantic
(^{2}H-depleted)
Alps
Ti, Si, Zr
Ti, Si, Zr
W. Med
(^{2}H-enriched)
G
Homogeneous marls
N
C
N. Atlantic moisture
(^{2}H-depleted)
ALPS
Increase in ^{2}H-enriched precipitations
Govone
PYRENEES
DINARIDES
APENNINES
Excess of W. Med. moisture
(^{2}H-enriched)
Evaporation: 3.0 - 4.0 mm/day
Evaporation: 4.0 - 8.0 mm/day
Strongly reduced connections
ATLAS
500 km
EARLY MSC PHASE

Figure 5